New solutions for combatting implant bacterial infection based on silver nano-dispersed and gallium incorporated phosphate bioactive glass sputtered films: A preliminary study

B.W. Stuart [a],[*], G.E. Stan [b], A.C. Popa [b],[c], M.J. Carrington [a], I. Zgura [b], M. Necsulescu [c], D. M. Grant [a]

[a] *Advanced Materials Research Group, Faculty of Engineering, University of Nottingham, Nottingham, NG7 2RD, UK*
[b] *National Institute of Materials Physics, Magurele, RO, 077125, Romania*
[c] *Army Centre for Medical Research, Bucharest, RO, 010195, Romania*

A B S T R A C T

Ag/Ga were incorporated into resorbable orthopaedic phosphate bioactive glasses (PBG, containing P, Ca, Mg, Na, and Fe) thin films to demonstrate their potential to limit growth of *Staphylococcus aureus* and *Escherichia coli* in post-operative prosthetic implantation. Dual target consecutive co-sputtering was uniquely employed to produce a 46 nm Ag:PBG composite observed by high resolution TEM to consist of uniformly dispersed ~5 nm metallic Ag nano-particles in a glass matrix. Ga^{3+} was integrated into a phosphate glass preform target which was magnetron sputtered to film thicknesses of ~400 or 1400 nm. All coatings exhibited high surface energy of 75.4–77.3 mN/m, attributed to the presence of hydrolytic P–O–P structural surface bonds. Degradation profiles obtained in deionized water, nutrient broth and cell culture medium showed varying ion release profiles, whereby Ga release was measured in 1400 nm coating by ICP-MS to be ~6, 27, and 4 ppm respectively, fully dissolving by 24 h. Solubility of Ag nanoparticles was only observed in nutrient broth (~9 ppm by 24 h). Quantification of colony forming units after 24 h showed encouraging antibacterial efficacy towards both *S. aureus* (4-log reduction for Ag:PBG and 6-log reduction for Ga-PBG≈1400 nm) and *E. coli* (5-log reduction for all physical vapour deposited layers) strains. Human Hs27 fibroblast and mesenchymal stem cell line *in vitro* tests indicated good cytocompatibility for all sputtered layers, with a marginal cell proliferation inertia in the case of the Ag:PBG composite thin film. The study therefore highlights the (*i*) significant manufacturing development via the controlled inclusion of metallic nanoparticles into a PBG glass matrix by dual consecutive target co-sputtering and (*ii*) potential of PBG resorbable thin-film structures to incorporate and release cytocompatible/antibacterial oxides. Both architectures showed prospective bio-functional performance for a future generation of endo-osseous implant-type coatings.

1. Introduction

The efficacy of conventional antibiotic treatments as a prophylactic measure for preventing post-surgery infection, in both the cases of metallic implant joint endoprostheses and dental fixtures (vastly based on titanium and titanium super-alloys, collectively accepted as gold standards), is declining due to the rise of resistant bacterial strains [1–3]. For instance, the UK National Joint Registry reported in 2020 that infections led to surgeries in 14.8% of primary hip replacement implants

that had an associated first revision [4]. Antibiotic loaded poly(methyl methacrylate) cements used to fix in place the titanium-based joint implants are no longer practical for the next generation of medical devices, which have advanced towards cementless, bioactive devices, intended to prolong implant fixation and minimise the foreign body response. Antimicrobial traits are similarly of high importance for dental implants, since the complete sterility of the oral environment cannot be achieved.

The application of thin films and thick coatings of bioceramic- and/

---

or bioglass-based materials on the surface of endo-osseous metallic implants, containing various antimicrobial agents, has recently emerged as a potent solution for this ever-growing healthcare system demand [5,6].

The most explored materials in this respect are either the phosphate-based (*i.e.*, calcium phosphates [7,8], phosphate glasses [9]) or phosphate-containing (silica glasses [10,11]), all having the advantage of absent or limited cytotoxic effects [7–11]. Plasma sprayed pure hydroxyapatite [HA, $Ca_{10}(PO_4)(OH)_2$] coatings have been clinically used since the 1980's, however, problems of poor biomimicry and mechanical spallation have been associated with varying crystallinity and inherent minimum coating thicknesses in the tens to hundreds of microns [12]. Novel technologies based on thin bioactive films, capable of combatting infection through the release of osteogenic and antimicrobial metals, are currently under investigation worldwide [13–17], relying on alternative deposition techniques, with the most prominent [18] being electrophoretic/electrochemical deposition [19], sol-gel [20], sputtering [21] and pulsed laser deposition [22].

Phosphate bioactive glass (PBG) thin films may function as therapeutic carriers by incorporating and subsequently releasing osteogenic elements such as Ca, P, and Mg to stimulate bone regeneration and enhance the fixation between the host tissue and the PBG coated implant [23–27]. The supplemental incorporation of antimicrobial agents could expand their biofunctionality. In this respect, in the framework of this study two effective antimicrobial elements [18,28] were selected: Silver (Ag) and Gallium (Ga).

The antimicrobial ability of Ag has been known since antiquity [29]. Ag is assumed to inhibit bacterial attachment during and post-surgery [28,30]. Only recently has its function been pinpointed to its release in form of ions from the erosion of nano-particulates in solution [30], opening the path towards a more precise design of implant constructs. However, cautionary measures need to be considered when employing Ag, since this specific antimicrobial is known to be biologically hazardous when found/released in large amounts [30,31]. Therefore, the application of very thin bio-functionalization layers (containing low to moderate contents of Ag) on the surface of metallic implants would be recommended.

Gallium [Ga (III)] ions have recently emerged as part of an alternate antibacterial strategy, due to their ability to disturb specific cellular processes (*i.e.*, metabolism and nutrition of microorganisms), as opposed to more conventionally available drugs which instead target biosynthesis of the cell wall or DNA replication [32]. Ga disrupts ferric iron-dependent metabolic pathways, and due to the importance of these in the bacterial physiology and pathogenicity, it has the potency to inhibit microbial growth [33,34]. In particular, bacteria mistake Ga^{3+} for Fe^{3+} which leads to cell degradation in response to an inability to reduce Ga^{3+} during redox cycling from Fe^{3+} to Fe^{2+}. Importantly Ga-containing agents have proven effective, *in vitro* and *in vivo*, even against pan-resistant (multidrug resistant) pathogens [32–36]. In particular, Ga has a greater half-maximum cytotoxic concentration with respect to Ag [18], therefore it could be used in thicker bioresorbable implant-type coatings, which in turn could stimulate the longevity and intensity of the antimicrobial-induced effect.

Ag [37–39] and Ga [40,41] have been incorporated only into bulk and powdered PBGs, synthesized by melt-quenching or peroxidation methods. No Ag- or Ga-containing PBG coatings with demonstrated bio-functionality have been reported to the best of our knowledge. Physical vapour deposition (PVD) techniques are attractive due to their propensity to generate high quality mechanically adherent and conformal thin films [26,42–45], and have been used to deposit PBG layers in the P_2O_5–MgO–CaO–Na_2O [46], P_2O_5–CaO–Na_2O–Fe_2O_3 [47], P_2O_5–MgO–CaO–Na_2O–Fe_2O_3 [14,28,48], and P_2O_5-ZnO-Nb_2O_5 [49] glass systems. The authors have recently reported on the compositional/thickness control, mechanical integrity and physical-chemical attributes of PBG coatings modified by Ga-doping and fabricated by radio-frequency magnetron sputtering (RF-MS) [50].

These scientific and technological state-of-the-art developments

[7–50] have motivated the search and delineation of new antimicrobial implant coating designs, relying on promising methodologies which can supersede the longstanding industrial standard of plasma sprayed thick coatings. Consequently, in the framework of this study, two independent antibacterial strategies based on magnetron sputtered PBG sacrificial layers are assessed and promoted for the future prevention of implant infections: (1) the dispersion of silver nanoparticles into the glass matrix by co-sputtering from two targets resulting in a composite coating; and (2) control over the duration of the antimicrobial efficacy by changing the thickness of the sacrificial Ga-doped PBG PVD deposited layer. The manufacturing routes advanced herein (*i.e.*, thin Ag:PBG composite layers or thicker Ga incorporated PBG coatings) aimed to utilise the ability of the additional constituting elements (*i.e.*, Ca, Mg, Na, and Fe) to tailor the cross-linking of phosphate glass units (as shown in Refs. [48, 50]) to achieve a suitable degradation timescale capable of facilitating the fast release of (*i*) Ag in its metallic form (known to possess lower systemic toxicity with respect to its ionic form [51]) from the composite layers or (*ii*) Ga^{3+} ions from the glass coatings, within the required 6–24 h window, and thereby to contribute to the prevention of post-operative infections.

2. Materials and methods

2.1. Target production

Two PBG sputtering targets, with a (mol%) composition given in Table 1, were produced by melt-quenching (MQ). Briefly, precursors of P_2O_5 (Thermo Fisher Scientific, Waltham, MA, USA; purity >98%), $MgHPO_4 \cdot 3H_2O$ (Sigma Aldrich, St. Louis, MO, USA; purity >97%), $CaHPO_4$ (Sigma Aldrich, St. Louis, MO, USA; purity >98%), NaH_2PO_4 (Sigma Aldrich, St. Louis, MO, USA; purity >99%), and $FePO_4 \cdot 2H_2O$ (Sigma Aldrich, St. Louis, MO, USA; reagent grade) or Ga_2O_3 (Sigma Aldrich, St. Louis, MO, USA; purity >99.99%) were ad-mixed (in the quantities listed in Table 1) and dehydrated at 450 °C in a Pt/Rh 90/10% crucible for 30 min. Each mixture was melted for 2 h at 1200 °C in air. The melts were cast at 450 °C into graphite moulds, and left to furnace cool. The moulds were chosen to produce P57-MQ and Ga-P51-MQ sputtering targets of 57 ± 1 and 76 ± 1 mm in diameter, respectively. To achieve the desired thicknesses, the base side of each target, to be positioned in contact with the magnetron cathode surface, was polished down to 6 ± 1 mm using isopropyl alcohol as a lubricant.

2.2. PBG films deposition by radio-frequency magnetron sputtering

In this work we aimed to explore the preliminary biological performance of two independent coating solutions, based on sacrificial antibacterial layers, for endo-osseous metallic implants. The two approaches differ in many respects (*e.g.*, thickness, antibacterial agent nature and chemical status), but their goal is the same: obtaining an antibacterial effect with reduced interference (if any) on eukaryotic cells.

A reduced thickness of the Ag:PBG composite sacrificial film was chosen to limit the release of silver within the medium and to maintain the leached concentrations below the known cytotoxic thresholds presented within the literature [52,53]. Knowing that the toxicity of Ga is far less than that of Ag [18], the manufacture of Ga-doped glass films of similar thickness to the Ag:PBG constructs would not be of high interest, as the exploration of the full potential of Ga could be missed. Consequently, in this second case, sputtered glass layers with thicknesses of one and two orders of magnitude higher were investigated.

The fabrication of the composite coating consisting of silver nanoparticle embedded PBG (further denoted as Ag:PBG-PVD) was carried out with a UDP 650 system (Teer Coatings Ltd., Droitwich, UK) equipped with a 13.56 MHz RF power source, using a dual-target consecutive magnetron co-sputtering process (see Fig. 1). The chamber was evacuated by consecutive rotary and diffusion pumping stages to a base pressure lower than 10^{-3} Pa. All depositions were conducted in 0.36 Pa

Table 1
Nominal oxide composition (mol%) of the PBG sputtering cathode targets and the quantities of precursors used for their preparation.

Target code	Nominal oxide composition (mol%)					
	P_2O_5	CaO	MgO	Na_2O	Fe_2O_3	Ga_2O_3
P57-MQ	57.0	12.0	14.0	14.0	3.0	–
Ga-P51-MQ	51.5	14.0	18.5	10.0	–	6.0
	Precursor (grams)					
	P_2O_5	$CaHPO_4$	$MgHPO_4 \cdot 3H_2O$	NaH_2PO_4	$FePO_4 \cdot 2H_2O$	Ga_2O_3
P57-MQ	38.3	15.5	18.3	29.0	8.4	–
Ga-P51-MQ	27.4	18.4	24.6	21.1	–	8.6
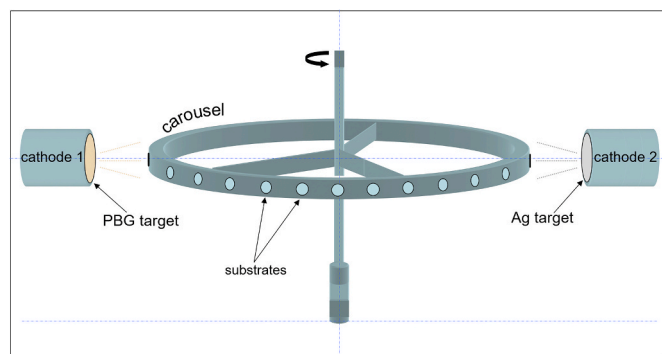
Fig. 1. Configuration employed in a TEERUDP-650 sputtering system to incorporate silver nano-particles into the PBG glass. The samples were fixed to a carrousel and continuously rotated past each cathode and target for consecutive deposition of the PBG matrix and silver particles. The process has been labelled here as "dual target consecutive magnetron sputtering".

of 99.999% (5 N) Pureshield Argon (gas flow of 125 sccm). The target-to-substrate distance was maintained as 40 ± 1 mm. Conditions and target potential/temperature were left to equilibrate for 30 min prior to commencing deposition by opening of the shutter. In order to incorporate Ag nanoparticles within the PBG thin film, a second Ag target (57 mm in diameter) was positioned parallel to the PBG target and separated by a distance of 580 mm. RF powers of 100 W and 5 W were set for the 57 mm diameter PBG and Ag targets, respectively.

The synthesis method for the production of the Ga-doped PBG films (further denoted as Ga-PBG-PVD), was presented in our previous work [50]. Here the deposition time was adjusted such as to produce batches of Ga-PBG-PVD films of two different thicknesses, *i.e.*, ≈ 400 and 1400 nm. For comparison, the main deposition conditions for each type of PBG-based layer are summarized in Table 2.

Certain precautions are required when dealing with soluble/resorbable implant coatings, since (*i*) the uniform stress distribution at the implant/bone interface can be radically and rapidly modified, leading to bone loss as a possible long-term result and (*ii*) *in situ* implant motion could be generated by the formed gap at the interface, leading to particulate debris which can cause foreign body chronic inflammatory reactions [54]. However, such worries should be significantly reduced (if not alleviated) by designs based on lower thickness coatings (with

Table 2
RF-MS deposition conditions used for the preparation of the Ag:PBG-PVD and Ga-PBG-PVD layers.

Layer type	Deposition conditions				
	Working gas	Sputtering pressure (Pa)	Power (W)		Target-substrate distance (mm)
			PBG	Ag	
Ag:PBG-PVD	Ar 5 N	0.36	100	5	40
Ga-PBG-PVD	Ar 5 N	1.33	60	–	40

respect to the commercial plasma sprayed ones), and thus conformal to the topography of the metallic implant surface. On the one hand, the overall stiffness and mechanical qualities of the metallic implant would be negligibly affected on a large-scale by the application of coatings with thicknesses in the range of tens to hundreds of nanometres, and thereby these coatings would also negligibly add to any induced stress shielding. On the other hand, in the case of the complete dissolution of the thin coating layer, the gap between implant and bone would be minimal (considering that implants are inserted into threaded holes or in bone shafts using low precision tools with positioning errors in the hundreds of micrometres), and thus, the *in situ* movements will be absent. For instance, deleterious effects on bone integration were recorded for amplitude of motions in the millimetre range [54], which definitely could not be the case here.

Both types of coatings were applied to mirror-polished (*i*) unalloyed commercially pure titanium (cp-Ti discs with diameter of ~10 mm diameter, thickness of ~0.82 mm, root square mean roughness of ~6 nm determined by as atomic force microscopy for surface areas of 10×10 μm^2) and (*ii*) silicon (Si wafers with size of 24×24 mm^2, thickness of ~0.45 mm, root square mean roughness of ~0.1 nm as determined by as atomic force microscopy for surface areas of 10×10 μm^2) substrates with a view to undertake (*i, ii*) physical-chemical analyses and (*i*) *in vitro* cytocompatibility tests and (*ii*) antibacterial assays.

2.3. Physical-chemical characterization

2.3.1. Fourier transform infra-red (FTIR) spectroscopy

The structure of the PBG powders (diluted in KBr to a ratio of 1:150) and films (deposited by RF-MS on IR transparent Si wafers) was investigated by FTIR spectroscopy in transmission mode, using a PerkinElmer Spectrum BX II spectrometer (PerkinElmer Corporation, Waltham, MA, USA). The FTIR spectra were collected in the wave numbers range 2000–550 cm^{-1}, at a resolution of 4 cm^{-1}, and represent the average of 64 individual scans.

2.3.2. Transmission electron microscopy (TEM)

Electron transparent transmission electron microscope (TEM) lamellae of Ag:PBG-PVD were prepared using a FEI Quanta 200 3D DualBeam FIB-SEM (FEI Company, Hillsboro, OR, USA) and a standard focused ion beam (FIB) lift-out method was employed. Representative TEM lamellae were taken directly from the as-deposited sample surfaces and platinum was deposited directly onto the coating surface in order to minimise the surface damage caused by subsequent FIB machining operations during sample preparation. A JEOL 2100F FEG-TEM (JEOL Ltd., Tokyo, Japan) operating at 200 kV was employed for conventional (parallel beam) bright field transmission electron microscopy (BF-TEM), high resolution transmission electron microscopy (HRTEM), bright field scanning transmission electron microscopy (BF-STEM), and elemental mapping via energy dispersive spectroscopy (EDXS-STEM). EDXS-STEM was performed using a 80 mm X-Max EDS detector (Oxford Instruments plc, Abingdon, UK).

2.3.3. Atomic force microscopy (AFM)

The surface topography of the PBG-based layers was examined by AFM, in non-contact mode, by using an NT-MDT NTEGRA Probe NanoLaboratory system (NT-MDT Spectrum Instruments, Moscow, Russia). A high-resolution silicon NT-MDT NSG01 cantilever was used, having a tetrahedral tip, with curvature radius of 6 nm and the cone angle at the apex of 7–10°. The AFM images were scanned over sample areas of 10×10 and 2×2 μm^2 and the root mean square roughness (R_{RMS}) has been determined.

2.3.4. Field emission scanning electron microscopy (FE-SEM)

The surface and cross-sectional morphology of the samples was surveyed by FE-SEM in high vacuum, using a Zeiss Gemini 500 (Carl Zeiss AG, Oberkochen, Germany), in secondary electron mode, at an acceleration voltage of 3 kV. No conductive coating was applied, to avoid concealing/obscuring the fine morphological details of the PBG-based specimens.

2.3.5. Energy dispersive X-ray spectroscopy (EDXS)

The composition of the P57-MQ and Ga-P51-MQ cathode targets and Ga-PBG-PVD sputtered films was assessed by EDXS. An INCA EDX microanalysis system (Oxford Instruments plc, Abingdon, UK) attached to a XL30 scanning electron microscope (Philips N.V., Amsterdam, Netherlands) was used. At least four composition analyses have been performed on randomly chosen regions of 30×30 μm^2 of each type of the PBG specimens, at an acceleration voltage of 15 kV.

2.3.6. X-ray photoelectron spectroscopy (XPS)

X-ray photoelectron spectroscopy (XPS) measurements were performed using a EscaLab Mark II spectrometer (VG Scientific, Waltham, MA, USA) with an Al K_α non-monochromatic X-ray source. The spectra were acquired at 20 mA and 12 kV emissions. All high resolution spectra were charge corrected with respect to adventitious carbon clearly defined at 284.8 eV.

2.3.7. Surface wetting measurements

The surface wetting properties of the Ag:PBG-PVD and Ga-PBG-PVD samples were investigated by static contact angle (CA) measurements, using a Drop Shape Analysis system, model DSA 100, from Krüss GmbH (Hamburg, Germany). All measurements were performed at room temperature, on at least four independent specimens, by applying the procedure described in Ref. [55]. Using CA measurements, the solid surface free energy (SFE) were calculated. MilliQ water and 1-Bromonaphtalene (Sigma Aldrich, St. Louis, MO, USA) were used as standard testing polar and dispersive liquids, respectively. The dispersive and polar parts of surface tension were obtained by using Owens–Wendt method for two test liquids [56].

2.4. Preliminary in vitro biological assessments

2.4.1. Degradation tests and inductively coupled plasma mass spectrometry analyses

Ag:PBG-PVD and Ga-PBG-PVD coated Ti samples were independently submerged in 1 mL of media [*i.e.*, deionized (DI) water, Dulbecco's Modified Eagle's Medium (DMEM), and Nutrient Broth (NB) of 1/3 Meat Bovine, 1/3 Yeast Extract, 1/3 NaCl formulation] in 20 mL polypropylene centrifuge tubes. The media was buffered at a pH of 7.4, and the assays were performed at a homeostatic temperature of 37 °C in a 5% CO_2 containing incubator. At time points 2, 4, 8, 16 and 24 h, the samples were diluted with 9 mL of ultra-pure water. The discs were removed and dried under a stream of compressed air. The remaining 10 mL of media was assessed by inductively coupled plasma mass spectrometry (ICP-MS) for degradation products using an iCAP-Q system (Thermo Fisher Scientific, Waltham, MA, USA).

The PBG film mass loss was assessed, prior to and after *in vitro* testing, using a MT5 micro-balance (Mettler Toledo, Columbus, OH,

USA) with a precision of a 0.001 µg. All experiments were performed in quadruplicates.

2.4.2. Cytocompatibility tests

The cytocompatibility was assessed in accordance with the ISO 10993-5:2009 standard [57]. The uncoated (control) and Ag: PBG-PVD, Ga-PBG-PVD, PBG coated Ti substrates were dry heat sterilized (180 °C/1 h). The samples were transferred in a laminar flow hood to sterile 24-well plates.

Human fibroblast cell (Hs27, ATCC® CRL-1634, Manassas, VA, USA) and mesenchymal stem cell (hMSC, Lonza, catalogue no. PT-2501, Basel, Switzerland) lines were used to test the cytocompatibility of the RF-MS PBG-based coatings. The Hs27 cell line was chosen due to the fibroblast's propensity in the human body and due to its implication in many tissue healing processes. Fibroblasts are known to possess interconvertibility [58], that allows them to change under adequate stimuli into any connective tissue cells, including cells of the bone. The hMSC line was selected due to its susceptibility to toxic environments, and its importance for longer term health of the tissue.

2.4.2.1. Cell culturing.

(a) The Hs27 cells were cultivated with DMEM with ʟ-glutamine, supplemented with 10% fetal bovine serum (FBS), penicillin (100 UI/mL) and streptomycin (100 µg/mL), in a humidified atmosphere incubator with 5% CO_2, at the homeostatic temperature of 37 °C. The confluent cells were detached with trypsin (2.5 g/L in phosphate-buffered saline without Ca and Mg (PBS, Sigma Aldrich, St. Louis, MO, USA)) and centrifuged at $250 \times g$ for 10 min, subsequent to trypsin inhibition. Then, the Hs27 cells were re-suspended in complete growth medium, and their concentration was set to 10^5 cells/mL with a Bürker-Türk counting chamber (Brand GmbH + CO KG, Wertheim, Germany). On each type of sample 100 µL of medium, containing 10^4 cells, was used. Further, the plates containing the cell seeded samples were transferred into a humidified incubator, and left for cell adherence. After 5 h, a volume of 400 µL of fresh cell culture medium was added in each plate well. Subsequently, the plates were transferred in the cell culture incubator, at 37 °C, 5% CO_2 humidified atmosphere, and the cells allowed to grow for 24 h.

(b) The hMSCs were subcultured according to manufacturer's instructions, and brought to confluence. The confluent cells were detached with trypsin (2.5 g/L in phosphate-buffered saline without Ca and Mg (PBS, Sigma Aldrich, St. Louis, MO, USA)) and centrifuged at $200 \times g$ for 10 min. hMSCs were resuspended in complete appropriate culture media (MSCGM human Mesenchymal Stem Cell Growth BulletKit™ Medium, Lonza, Basel, Switzerland). The cell number was adjusted to 10^5 cells/mL, using a Bürker-Türk counting chamber (Brand GmbH + CO KG, Wertheim, Germany). On each sample 100 µL of medium, containing 2×10^3 cells, was spread and the plate was transferred in the incubator. After 4 h, 400 µL of fresh cell culture medium was added in every well and the plates were transferred in the cell culture incubator, at 37 °C, 5% CO_2 humidified atmosphere.

2.4.2.2. Cell morphology.

Morphological features of the cells cultured on the uncoated and coated Ti substrates were inferred by fluorescent microscopy using a Zeiss Axioplan microscope (Carl Zeiss AG, Oberkochen, Germany) with appropriate filters. The cells were fixed with 4% para-formaldehyde dissolved in PBS for 15 min at room temperature. After washing three times with PBS, the actin cytoskeleton was stained using 100 µL of phalloidin-AlexaFluor546 (Invitrogen, Carlsbad, CA, USA) and each sample incubated for 1 h. Further, the samples were washed using three consecutive cycles of 15 min, and then incubated

with 1 μg/mL of DAPI (4′,6-diamidino-2-phenylindole) for nuclei counterstaining. The samples were washed two times with PBS and once with double distilled water (15 min for each wash) and mounted onto 0.17 mm glass coverslips using the Dako (Invitrogen, Carlsbad, CA, USA) mounting medium in view of cell morphological investigation.

2.4.2.3. Cell toxicity by LDH assay. After 24 h of cell culturing, the medium supernatant was collected in order to evaluate the cytotoxicity of the PBG-based coatings by the lactose dehydrogenase (LDH, Thermo Fisher Scientific, Waltham, MA, USA) assay. Into wells with 50 μL of medium were added aliquots of 50 μL of LDH assay buffer, and the plates transferred into the incubator for 30 min. Then, the reaction was terminated by addition of 50 μL of stop buffer. The absorptions were read at wavelengths of 490 nm and 620 nm using a Zenyth 3100 multimode microplate reader (Anthos Labtec Instruments, Salzburg, Austria). The cell death was inferred by subtracting the 620 nm values from the 490 nm ones. The control of the experiment for LDH activity was represented by the fresh complete medium.

2.4.2.4. Cell proliferation by MTS assay. The cell proliferation on the surface of the uncoated and PBG-coated Ti substrate was assessed via 3-(4,5-dimethylthiazol-2-yl)-5-(3-carboxymethoxyphenyl)-2-(4-sulfo-phenyl)-2H-tetrazolium (MTS, Promega Corporation, Madison, WIS, USA) assay. First, 400 μL of DMEM was added to each well and incubated for 30 min. Next, 80 μL of MTS containing buffer was added and further incubated for 1 h in the incubator. The plates were gently stirred and agitated for 1 min at 150 rotations/min. Then, a 120 μL aliquot was collected from each sample well and moved into a 96 well plate. The absorption was read at a wavelength of 490 nm using the same Zenyth 3100 multimode microplate reader (Anthos Labtec Instruments, Salzburg, Austria). Unless indicated, all the cell culture reagents were acquired from Sigma Aldrich (St. Louis, MO, USA).

2.4.3. Antibacterial assays

The antibacterial effect of the samples was carried out in accordance with the ISO 22196:2011 standard [59]. The antibacterial efficacy of RF-MS PBG-based coatings was tested against both Gram-positive (*Staphylococcus aureus*, ATCC® 6538, Manassas, VA, USA) and Gram-negative (*Escherichia coli*, ATCC® 8739, Manassas, VA, USA) strains. *S. aureus* and *E. coli* are pathogen agents known to frequently cause post-surgery infections in both orthopaedics and dentistry [3, 60–67].

First, the square PBG coated Si substrates were dry-heat sterilized (180 °C/1 h) and transferred into sterile 6-well plates in the laminar flow hood. Suspension of *S. aureus* and *E. coli* in nutrient broth (NB) were independently prepared to a concentration of 10^6 colony forming units (CFU)/mL by viable cell count. 100 μL of NB, containing 10^5 viable CFUs was layered atop the coated samples and an inert sterile plastic film (square with 20 mm side) was placed over the liquid, as described in the ISO 22196:2011 standard. The plates were transferred in the incubator. After 24 h of incubation, 3 mL of NB were added in each well and the plastic film and samples were thoroughly scraped with a dedicated sterile rubber scrapper to detach all the bacterial cells that might be encapsulated in biofilm (ultrasonication of samples was avoided since it can affect the viability of bacterial cells, and thereby, the CFU analysis will become inaccurate). 10-fold serial dilutions were prepared for each situation, and from each sample dilution two pre-casted plates with plate count agar (100 mm diameter) were seeded with 1 mL inoculum. After 24 h in the incubator the plates were counted for colonies. The number of viable CFU present after 24 h of incubation in the presence of the Ag:PBG-PVD, Ga-PBG-PVD or controls were calculated with the formula: Viable CFU = 3 × dilution × (average number of colonies on the two plates). All materials used in antimicrobial tests were from Sanimed International Impex, IVD (In Vitro Diagnostics) (Bucharest, Romania) certified producer for medical bacteriology laboratories.

2.4.4. Statistical analysis

All *in vitro* biological experiments were performed (at least) in triplicate. The results are presented as arithmetic average ± standard error of the mean. The statistical analyses were performed using the unpaired Student's t-tests or one-way Anova followed by a Tukey Kramer post hoc test (when appropriate), and the differences were considered significant when $p < 0.05$.

3. Results and discussion

3.1. Physical-chemical characterization

The physical-chemical analysis of the Ga-PBG-PVD coatings was partly addressed in our previous work [50]. For this reason, the current study will focus predominately on the morphological, structural and chemical features of the Ag:PBG-PVD type coating, with additional characterization added where appropriate in the case of the Ga-PBG-PVD samples.

3.1.1. Structural characterization

The FTIR spectra of the Ag:PBG and Ga-PBG targets and deposited films are presented comparatively in Fig. 2. All materials featured equivalent IR absorption bands, peaking at similar wave number positions, but with dissimilar intensities. Explicitly, the observed IR can be ascribed as follows [47,50,68,69]:

- ~790–740 cm^{-1}: symmetric stretching (ν_s) of P–O–P bridges in the Q_P^1 and Q_P^2 phosphate units;
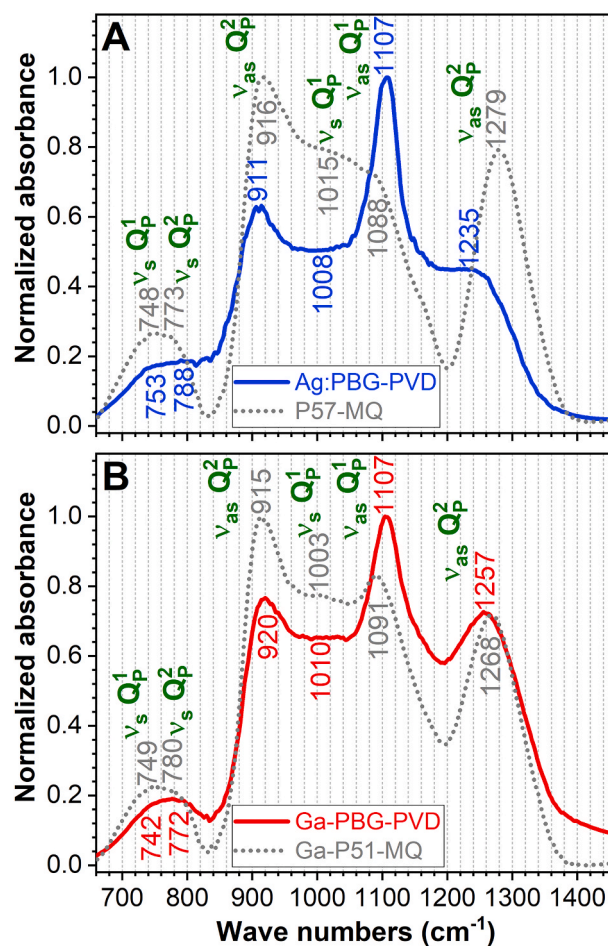

Fig. 2. Comparative FTIR spectra of the magnetron sputtered (A) Ag:PBG and (B) Ga-PBG films and of their corresponding source materials (cathode targets).

- ~930–900 cm^{-1}: asymmetric stretching (ν_{as}) of P–O–P bridges in the metaphosphate Q_P^2 units;
- ~1150–1080 cm^{-1}: ν_{as} of the end-of-chain $(PO_3)^{2-}$ in the pyro-phosphate Q_P^1 units;
- ~1280–1230 cm^{-1}: ν_{as} of non-bridging oxygen (NBO) atoms of O–P–O bonds, middle-of-chain $(PO_2)^-$, and terminal oxygen bonds (P=O) in the metaphosphate Q_P^2 units.

Both types of PVD film exhibited a lower degree of glass network connectivity with respect to each corresponding source material, as evidenced by the increase in intensity of the ν_{as} Q_P^1 bands at the expense of the ν_{as} ones appertaining to bonds in Q_P^2 units. It is thus suggested an incongruent target-to-substrate atomic transfer of the network glass formers (*i.e.*, P), a characteristic of the RF-MS processes [48]. A more salient depolymerization was noticed in the case of Ag:PBG-PVD, as expected for films deposited under low sputtering pressure regimes [48].

The depolymerization induced by this methodology is ideal where PBG sacrificial implant coatings are being designed with rapid bio-degradation in intercellular fluids, and thus capable of readily releasing the antimicrobial agents embedded within their glass matrix. Such a feature could be of paramount importance, as the first hours post-implantation are known to be critical for preventing infection, while the bacteria are still dormant and metabolically inactive, and thereby easier to combat [70,71].

3.1.2. Cross-sectional morphology analysis

A FIB prepared lamella was imaged by BF-TEM (Fig. 3A), indicating a coating thickness for Ag:PBG-PVD of 46 ± 1 nm. The BF-STEM image

and the corresponding EDXS mapping suggested a uniform dispersion of Ca and scattered distribution of Ag particulates throughout the cross-section (Fig. 3B). P was not measured due to overlap of the Pt K_α X-ray emission from the deposited Pt band during the FIB lift-out pro-cedure. The Ag:PBG-PVD thin film (cross-sectional) growth morphology appeared granular (Fig. 3A and B). The FE-SEM cross-sectional imaging indicated that both the Ga-PBG-PVD ≈400 nm (Fig. 3C) and Ga-PBG-PVD ≈1400 nm (Fig. 3D) coatings elicited a smooth growth morphology composed of fine columns, characteristic of amorphous films deposited by RF-MS [45]. Thereby, the growth morphology of the Ag:PBG-PVD films differed significantly from the columnar-type observed in the Ga-PBG-PVD layers, which is ascribed to the employed argon pressure and substrate temperature regimes, according to the Thornton structure zone model [72]. The columnar growth is known to be preserved only for low Ag contents (<8 at.%); at higher concentra-tions, Ag disturbs the columnar growth, segregates and forms agglom-erates, leading to a granular-type morphology [73].

The HRTEM analysis (Fig. 3E) revealed that Ag was efficaciously incorporated into PBG matrix by the "dual target consecutive co-sput-tering" process, in form of spherodised (dark contrast) crystalline nano-particles (NPs) with sizes in the range of 4–6 nm. The HRTEM micro-graph (Fig. 3F) and the corresponding Fast Fourier Transform (FFT) diffraction pattern (Fig. 3G) confirmed that the crystalline NPs are fcc-Ag (space group: Fm3m) and indexes to fcc-Ag taken along the [0 –1 1] zone axis. It is suggested that Ag was condensed independently from the PBG, creating the dispersion of Ag NPs embedded into the PBG matrix. This effect was caused by the unique sputtering configuration and parameters used for co-sputtering such that the cp-Ti substrates
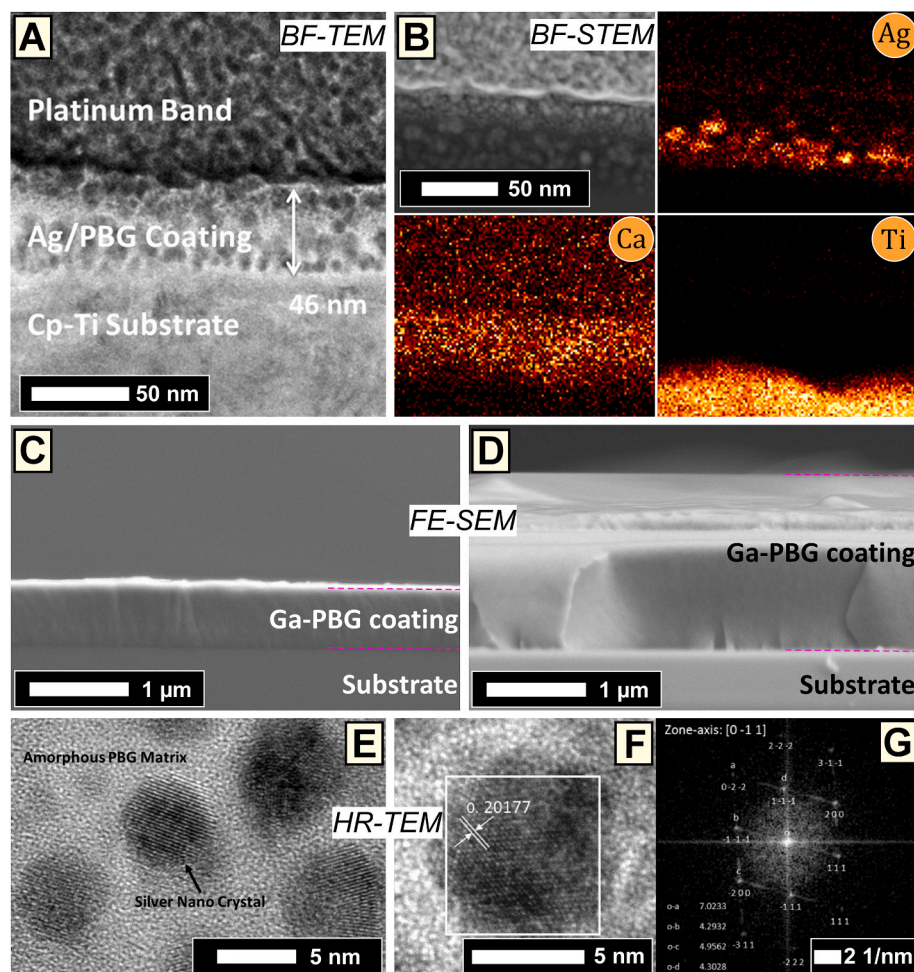
Fig. 3. (A) Cross-sectional BF-TEM micrograph of the Ag:PBG-PVD/Ti thin film (thickness of ~46 nm); (B) Cross-sectional BF-STEM image of the Ag:PBG-PVD/Ti specimen accompanied by EDXS elemental distri-bution maps of Ag, Ca, and Ti. (C,D) Cross-sectional FE-SEM representative images of the Ga-PBG-PVD/Si coating at a thickness of (C) ≈400 and (D) ≈1400 nm. (E) HR-TEM micrograph of an Ag:PBG-PVD/Ti thin film FIB lamella, highlighting the even dispersion of Ag nano-crystals within an amorphous PBG matrix. (F) HR-TEM image of a single silver nano-crystal, where (G) illustrates the accompanying FFT of the region marked in (F). The FFT presented in (G) indexes to Ag [0 –1 1].

were independently rotated past both the PBG and Ag targets allowing for consecutive and repetitive condensation of a PBG followed by Ag at minimal radio-frequency deposition power of 5 W (*see* Section 2.2).

3.1.3. Surface morphology analysis

The AFM surface morphology analysis (Fig. 4i-A-H) was performed for films deposited on the topologically defect-free mirror-polished Si substrates with R_{RMS} values < 0.1 nm (Fig. 4i–A). This allowed for the identification of the morphological features of the films independently of those of the substrate. The Ti substrates, even if generally smooth ($R_{RMS} \approx 6$ nm) were found to contain sporadic craters (data not shown), as a result of the polishing process, due to the softer nature of Ti with respect to Si. The Ag:PBG-PVD films had a granular surface morphology consisting of round-shaped small particulates, on top of which, were rare larger-sized particles (Fig. 4i–B). Their surface (R_{RMS}) roughness was ~2 nm. The high magnification FE-SEM investigations (Fig. 4ii-A′) confirmed the presence of the two type of particles, of ~9 and 30–65 nm, with the larger ones strongly enriched in Ag (Fig. 4ii-B′). The formation of larger Ag particulates on the sample surface, at the end of the coating process, with respect to those immersed in the film matrix (Fig. 3E) is not unprecedented [73]. It is believed that during a constant deposition process, marked by a continuous influx of target sputtered species, the nucleated Ag NPs will be enwrapped, and their growth will be hindered [73]. However, at the end of the deposition, when no more PBG *ad*-atoms are arriving, the silver will be allowed to migrate and agglomerate to lower surface energy sites [73], giving rise to larger formations. The Ga-PBG-PVD coatings (Fig. 4i-C-F; Fig. 4ii-C') presented the familiar morphology of the sputtered PBG layers, featuring surface pits [47,50]. The surface pits are attributed to an inadequate diffusion of the arriving

ad-atoms, higher volatility of P_2O_5 with respect to the other glass constituents, and self-shadowing phenomena [47,50]. With the increase of the Ga-PBG-PVD film thickness, the surface pits become larger (increasing from ~300 to ~570–1100 nm) and deeper (the depth augmenting from ~4 to ~19 nm) (Fig. 4i–G,H), suggesting that the self-shadowing role becomes more prominent, with the pits created in earlier deposition steps further impeding the diffusion of sputtered species on the growing film surface. This resulted in an increase in the surface roughness (R_{RMS}) from ~1.5 nm (irrespective of size of scanned area) to ~8 and 12 nm (for scanned surface areas of 10×10 and 2×2 μm^2), in the case of Ga-PBG-PVD≈400 nm and Ga-PBG-PVD≈1400 nm, respectively.

3.1.4. Chemical analysis (EDXS and XPS)

The composition of the as-fabricated cathode targets was confirmed by EDXS-SEM (Table 1 vs. Fig. 5i–A,B). The oxide concentration of the PVD films (reconstituted based on the EDXS-STEM and EDXS-SEM elemental quantitative analyses for the Ag:PBG-PVD and Ga-PBG-PVD films, respectively) indicated a loss of P_2O_5 with respect to the source materials, as hinted by the FTIR spectroscopy results (Fig. 2). The Ag: PBG-PVD film consisted of 64.5 wt% PBG and 35.5 wt% Ag.

The target-to-substrate stoichiometric deviations and their causality were well-documented in our previous studies [46–48,50], undertaken to define a reproducible magnetron sputtering protocol for the deposition of PBG layers. Briefly, these compositional changes are primarily the result of preferential sputtering effects due to differential scattering of constituent elements by the working gas as well as to variations in dissociation energies of the target structural units and atoms. The re-sputtering of deposited atoms by the high energy incident sputtered
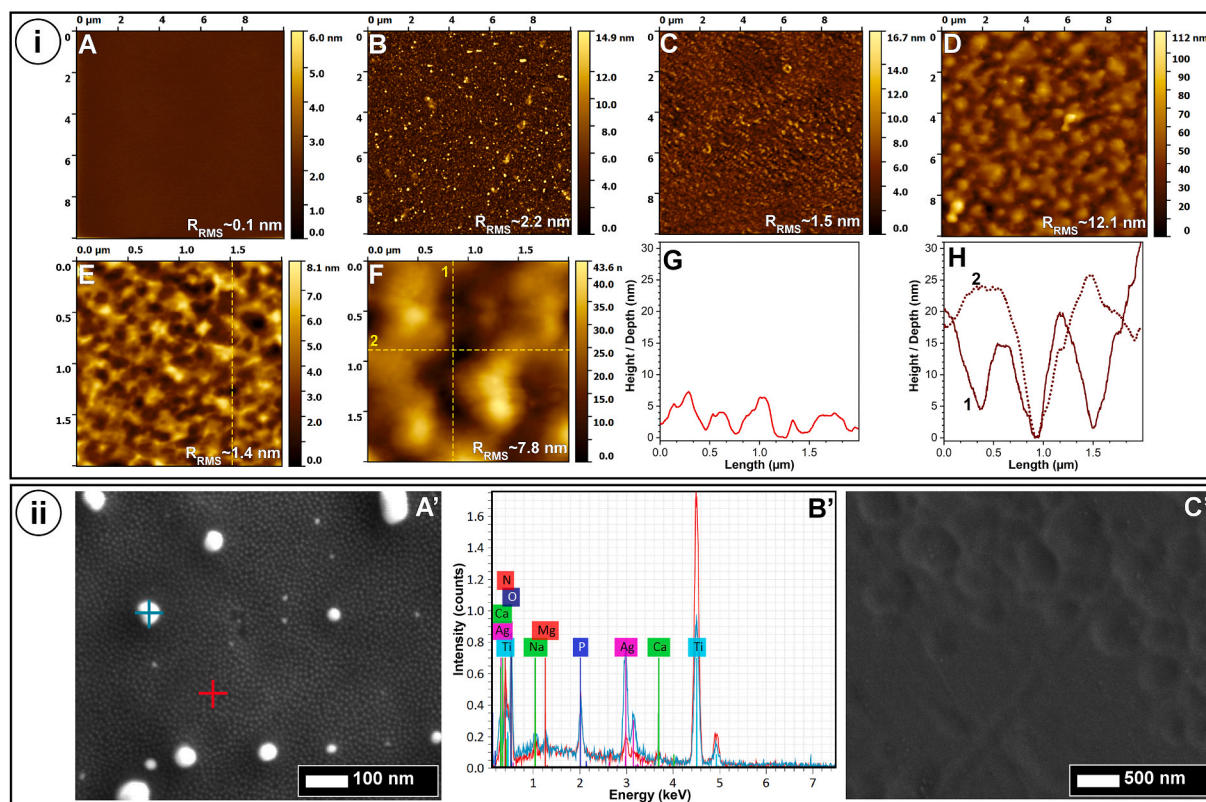
Fig. 4. (**i**) AFM images of the mirror polished Si substrate (**A**) before and (**B–F**) after coating with (**B**) Ag:PBG-PVD, (**C,E**) Ga-PVD-PBG≈400 nm, and (**D,F**) Ga-PVD-PBG≈1400 nm type layers, recorded on surface areas of (**A–D**) 10×10 μm^2 and (**E,F**) 2×2 μm^2. The R_{RMS} value is inserted in each corresponding AFM micrograph. (**G,H**) Comparative height profiles of the corresponding dashed lines drawn in the (**E**) and (**H**) AFM images, respectively. (**ii**) FE-SEM images of the (**A′**) Ag:PBG-PVD and (**C′**) Ga-PVD-PBG≈1400 nm type layers grown on mirror polished Ti substrates. (**B′**) Point EDX spectra acquired for the Ag:PBG-PVD/Ti sample at the zones highlighted in (**A′**): film matrix region - red line; light-coloured nano-particle: cyan line. (For interpretation of the references to colour in this figure legend, the reader is referred to the Web version of this article.)
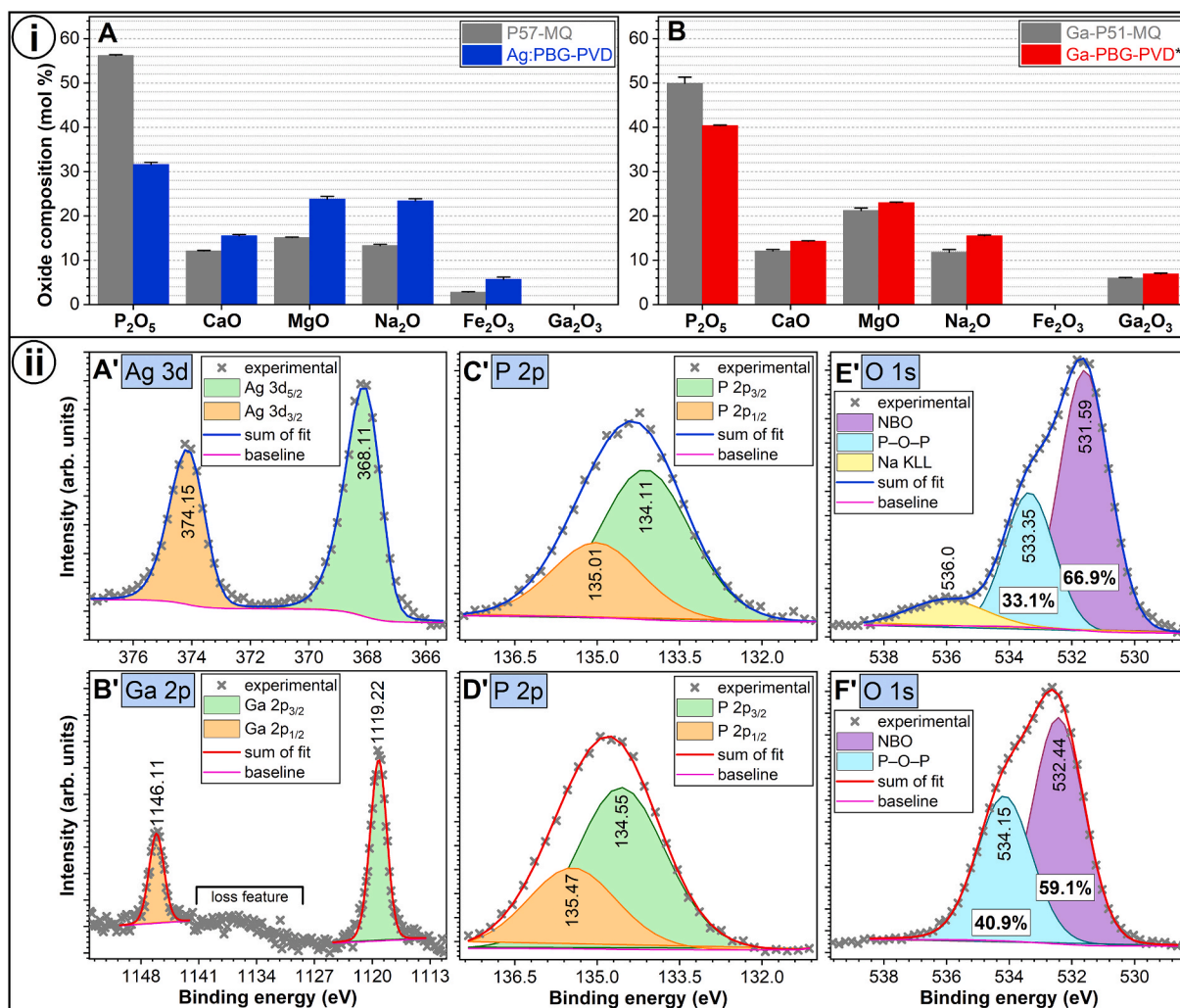
Fig. 5. (i) Comparative experimental oxide compositions of the magnetron sputtered (**A**) Ag:PBG and (**B**) Ga-PBG films and of their corresponding source materials (cathode targets), as estimated based on EDXS-type analyses. The results are presented as mean ± standard error of the mean (n = 4). *Ref. [50]. **(ii)** XPS spectra of (**A′**) Ag 3d, (**B′**) Ga 2p, (**C′, D′**) P 2p and (**E′, F′**) O 1s photoelectron core level peaks, indicative of surface bonding state, recorded for the (**A′, C′, E′**) Ag:PBG and (**B′, D′, F′**) Ga-PBG PVD films.

units (atoms or clusters) should be also more pronounced at low working gas pressures and/or high deposition powers. In such a case, the P content is the most susceptible to being ill-replicated in the films, since P requires more energy to form stable oxide bonds (*i.e.*, 2983 kJ mol^{-1}) with respect to the other glass elements [48], leading to weaker surface bonding, and therefore easier susceptibility to re-sputtering. This behavioural pattern seems to support the lower P_2O_5 content of the Ag: PBG-PVD coatings (deposited at lower argon pressure of 0.36 Pa and higher sputtering power of 100 W) with respect to the Ga-PBG-PVD ones (deposited at a higher argon pressure of 1.33 Pa and lower sputtering power of 60 W) (Table 2).

The XPS analysis was used to assess the chemical state of the antimicrobial agents and the surface structure of the sputtered glass films. The binding energy location of the Ag $3d_{5/2}$ and Ag $3d_{3/2}$ photoelectron emission lines at 368.11 and 374.15 eV (Fig. 5ii-A) was most closely associated with metallic Ag [74–78], as expected from condensation in the inert argon environment and as clearly indicated by TEM analysis. The binding energy of the Ga $2p_{3/2}$ (1119.22 eV) and Ga $2p_{1/2}$ (1146.11 eV) (Fig. 5ii-B) confirmed their complete oxidation [79–81].

The position of the P $2p_{3/2}$ line at 134.11–134.55 eV was found to be at an intermediate location between the associated position for meta- and pyro-phosphate structures (Fig. 5ii-C,D), suggesting the combined presence of metaphosphates (PO_3) and pyrophosphates (P_2O_7) [46,74,

82,83]. The decrease of the P 2p binding energy, recorded in the case of Ag:PBG-PVD, indicated an increase in the network modifier concentration, in good agreement with the EDXS analyses (Fig. 5i). In such a case, two outcomes are foreseen [84–86]:

(1) The network connectivity of the PBG will be decreased, leading to the generation of NBOs. This depolymerization process of the phosphate chains will be accompanied by a transfer of electronic changes, and consequently an increase of electronic density around P and therefore, a decrease in the P 2p binding energy.

(2) At a high concentration (typically ≥50 mol%) of network modifiers the disruption of the P=O linkages can be expected. One should note that the charge distribution in the P=O bond is displaced toward oxygen, suggesting an electron density deficiency around P and thereby, a reduction of the nuclear charge shielding. When the P=O is cleaved, the electron density around P may increase, resulting in the decrease of the P 2p binding energy.

Both hypotheses are supported by a more drastic decrease of the asymmetric stretching IR absorption bands of middle-of-chain (PO_2)$^-$ and terminal oxygen bonds (P=O) in the metaphosphate units, noticed in the case of Ag:PBG-PVD with respect to Ga-PBG-PVD (Fig. 2).

Previous investigations showed that polymerisation by production of

metaphosphate species led to increased wettability, water adsorption and therefore degradation [14].

Furthermore, the O 1s core level can be deconvoluted with two components [87], one positioned at higher binding energies, assigned to the bridging P–O–P oxygen atoms, and a second one, situated at a lower binding energies, including two types of terminal/non-bridging oxygen atoms (P=O and P–O–M, where M = network modifier). The chemical shift of the latter two is too small to be reasonably separated under the employed measurement (resolution) conditions. The peak separation procedure applied to the O 1s core level (Fig. 5ii-E,F) confirmed the higher depolymerization degree of the Ag:PBG PVD films, having a NBO content of ~67%, with respect to Ga-PBG-PVD which amassed ~59% NBOs.

3.1.5. Surface energy measurements

Surface free energies of the uncoated and PBG-coated cp-Ti substrates were measured before and after degradation for 4 h in H_2O. The application of the PBG coating on mirror-polished cp-Ti resulted in a super-hydrophilic surface (*i.e.*, the CA with water being equal or close to zero degrees), with the complete spreading of water on the specimens (Fig. 6A). This behaviour can be connected with high solubilisation (by hydrolysis) ability of these particular PBG formulations, with the water molecules being rapidly absorbed and reacted leading to the formation of OH^- groups on the coating surface [88]. The presence of the surface pits (Fig. 4) may be a concurrent factor, allowing the infiltration of liquid inside coatings through the capillary action [88]. After 4 h of

soaking in water the CA values remain unaltered (Ga-PBG-PVD 1400 nm) or increased to 10° (for Ag:PBG-PVD) and 26° (for Ga-PBG-PVD 400 nm). Hydrophilic-type implant surfaces as these are known to facilitate the cells adhesion, migration and proliferation, to the benefit of a fast bone tissue regeneration [89].

The hydrophilicity of the PBG coatings was additionally supported by the superior surface free energy values (Figs. 6B), 71–78 mN/m, compared to the uncoated mirror polished cp-Ti (~44 mN/m).

3.2. Preliminary in vitro biological assessments

3.2.1. Degradation and ion release profiles

The thinness of the Ag:PBG-PVD films (≈46 nm) limited the mass of the film to below the reliable resolution of the microbalance and therefore the mass loss/degradation profile could not be measured. The mass loss profiles for Ga-PBG-PVD (≈1400 nm) were significantly different in DI water, NB and DMEM as presented in Fig. 7A. Specifically, the fastest degradation and leaching of PBG components was observed in NB for which Ga-PBG-PVD was fully dissolved following 8 h of immersion. It should be noted that all variations of PBG-coated samples were extracted clean from the NB solution, as featured by the glossy mirror-polished surface of the metallic Ti substrate, without traces of film (and its specific colour) on the entire specimen surface. In DI water the coating exhibited slightly different values with similar trends, progressively increasing up to 8 h, followed by stabilisation at 72% mass loss.

Degradation was markedly different in DMEM where a reduction in mass of 16% was observed after 1 h of immersion, remaining stable at *ca.* 20% thereafter up to the final measurement time of 24 h. This could have been attributed to the following two factors: (*i*) the higher pH buffering capacity of DMEM and (*ii*) formation of a shielding layer of adsorbed organics, amino-acids and serum proteins on the surface which is well-documented in literature to cause a lag in surface dissolution [90].
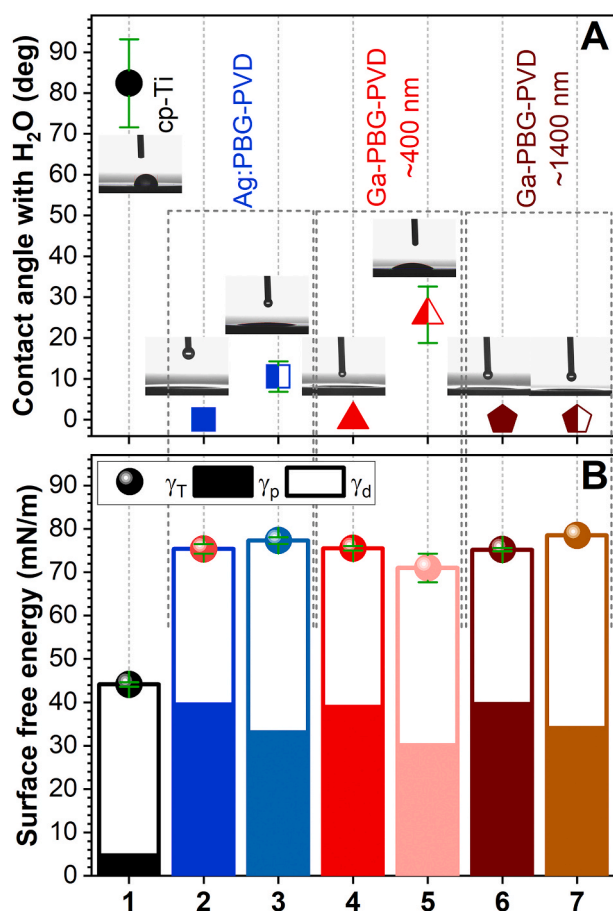

Fig. 6. (A) Average water contact angles and representative captured screen shots and (B) surface free energy values recorded for (1) mirror-polished cp-Ti and (2, 3) Ag:PBG-PVD, (4, 5) Ga-PBG-PVD≈400 nm and (6, 7) Ga-PBG-PVD≈1400 nm films, (1, 2, 4, 6) as-prepared and (3, 5, 7) after 4 h of degradation in water. Note: γ_T – total surface free energy, γ_p – polar component, and γ_d – dispersive component.
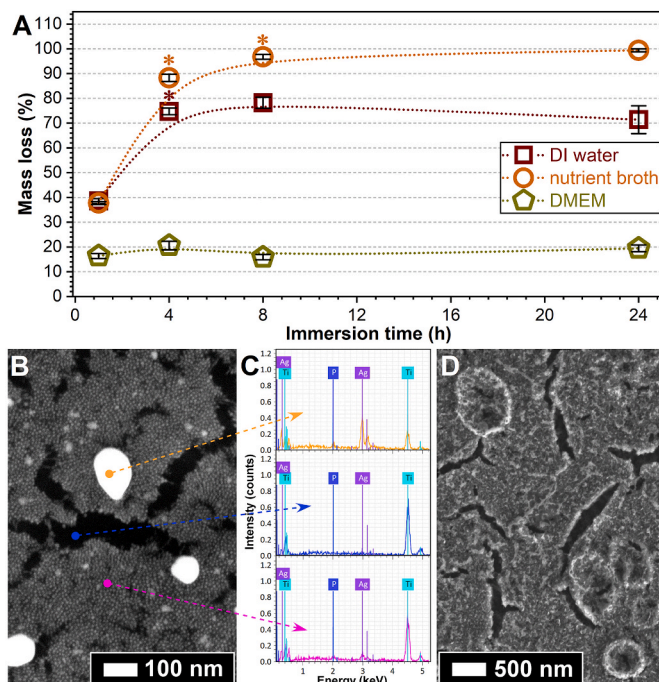

Fig. 7. (A) Mass loss temporal profiles recorded for Ga-PBG-PVD≈1400 nm samples in DI water, NB and DMEM (*$p < 0.05$, one-way ANOVA followed by Tukey Kramer's post hoc test). (**B,D**) FE-SEM images of the Ag:PBG-PVD and Ga-PBG-PVD≈1400 nm layers deposited onto mirror-polished Ti, soaked in DMEM solution for 24 h. (**C**) Point EDX spectra collected in the zones highlighted with arrows in (**B**), for the Ag:PBG-PVD/Ti thin film degraded for 24 h in DMEM.

Any hypothesis of biomineralization occurring here (*i.e.*, formation of amorphous calcium phosphate deposits which could crystallize in time into a carbonated hydroxyapatite) in such a short period of time (*i. e.*, 1 day) on the surface of PBG layers, thereby stalling their degradation in DMEM, should be excluded. PBGs are relatively high-solubility materials [9,14], and biomineralization has only been reported in a single case by Gayathri Devi et al. [91]. However, this took place for bulk PBG specimens after 20 days of immersion in a testing medium with higher Ca/P molar ratio (*i.e.*, Kokubo's simulated body fluid, Ca/P = 2.5 [92]) with respect to the complex organic-inorganic DMEM medium (Ca/P $\approx$1.99) [93]).

The FE-SEM & EDXS surface analyses (Fig. 7B–D) confirmed that no calcium phosphate deposits were formed. The morphology of calcium phosphates grown in biomimetic conditions is an unambiguous one, consisting of acicular needles agglomerated into spheroids with sizes in the micrometre range [90,92]). Instead, the FE-SEM images have indicated the remaining topography of the sputtered layers, and, their original globular and pitted morphology, for both Ag:PBG-PVD (Fig. 7B) and Ga-PBG-PVD (Fig. 7D), respectively (Fig. 4ii-A′,C′). Signs of film erosion were also evident, as well as cracks through which the Ti substrate was visualised (Fig. 7 B vs. Fig. 7C). These film cracks are known to occur, usually associated with the drying process of the soaked samples [94], then to a preferential local film dissolution.

The ion release profiles for P, Ca, Mg, Na, Ag and Ga in DI water, NB and DMEM are presented in Fig. 8. The overwhelming presence of P, Ca, Mg and Na within DMEM and NB compared to the low volume of Ag: PBD-PVD within the thin film prevented reliable detection of the listed ions. As such only Ag^{2+} could be quantified. Degradation in DI is a standard approach for assessing degradation of bio-resorbable glasses to isolate the hydrolytic dissolution mechanisms and to determine the effect on coating stability relative to compositional/structural modifications [95–97]. The ICP-MS results suggested that the glass was entirely dissolved by 1 h (P $\approx$6 ppm; Ca $\approx$2 ppm; Mg $\approx$1.1 ppm; Na $\approx$2.5 ppm; Fe $\approx$0.5 ppm), showing no further degradation up to 24 h. There was no identifiable Ag^{2+} release in DI water or DMEM suggesting that metallic silver was insoluble at the employed testing conditions. In contrast, in NB, Ag was progressively released following dissolution of the glass matrix for which concentration ranged from 3 to 9 ppm, over the 1–24 h period.

The ion release profiles for Ga-PBG-PVD films were well-aligned with mass loss results presented in (Fig. 8). The PBG components (*i.e.*, P, Ca, Mg, Na and Ga) were rapidly released in DI water and NB during the first 4 h of incubation. In DMEM the ion release profiles were significantly

lower than found in DI water and NB (exemplified by the dissolution of phosphate glass backbone to P ions which ranged from ~57, ~263 and ~54 ppm in DI water, NB and DMEM respectively). Ga^{3+} ion released concentrations in DI water, NB and DMEM were 5.5, 27.3 and 3.7 ppm, respectively.

Although both DMEM and NB are media with important organic components, they each induce different film dissolution trends. This effect can be attributed to the decrease in pH typically observed when PBG dissolves in aqueous media to form phosphoric acid. This is combined with the higher acid buffering capacity of DMEM, which is designed to maintain pH value of 7.25 for up to 72 h when cells are cultivated in a 5% CO_2 atmosphere. As the microbiology nutrient broth contains chloride ions (with respect to DI) and no pH buffer (with respect to DMEM), it will lead to a faster glass dissolve and readily release of ionic constituents. The varying dissolution speeds in NB (observed here) and the wide variety of cell culture media (reported in literature) is problematic as it could likely foster the occurrence of misleading *in vitro* antimicrobial studies. As shown here media properties can lead to higher degradation and thereby a higher concentration of released therapeutic ions. Whilst a methodology does not yet exist to truly mimic the biological environment, continual development of in-depth testing methods is required from the biomaterials community.

The opinion of the authors is that a significant development step in degradation/ion release testing could be to use a complex standard DMEM with 10% fetal bovine serum, therefore better mimicking the environment found *in vivo*, instead of deionized water or other pure inorganic solutions such as Kokubo's simulated body fluid or TRIS-HCl buffer. A modification to the antibacterial assay ISO 22196:2011 could also be envisaged by replacing the classic nutrient broth with the same DMEM fetal serum supplemented solution (used for the cytocompatibility tests). This could allow for a unitary testing and a better understanding of biomaterials behaviour, leading to a more reliable selection of material candidates for future *in vivo* studies. However, an important aspect needs to be considered when designing an implant coating. As bacteria develop in the proximity of the implant the environment will become more acidic, causing an increase in film dissolution and release of therapeutic ions, which will accelerate the antimicrobial activity required.

The remarkable property of PBGs to have a low pH acting as a switch for dissolution resulting in therapeutic ions released from the glassy network, might prove of extreme importance since it is well-known that conventional antibiotics lose their potency in the acidic environments as a result of microbial infections and bacteria metabolism. The potential
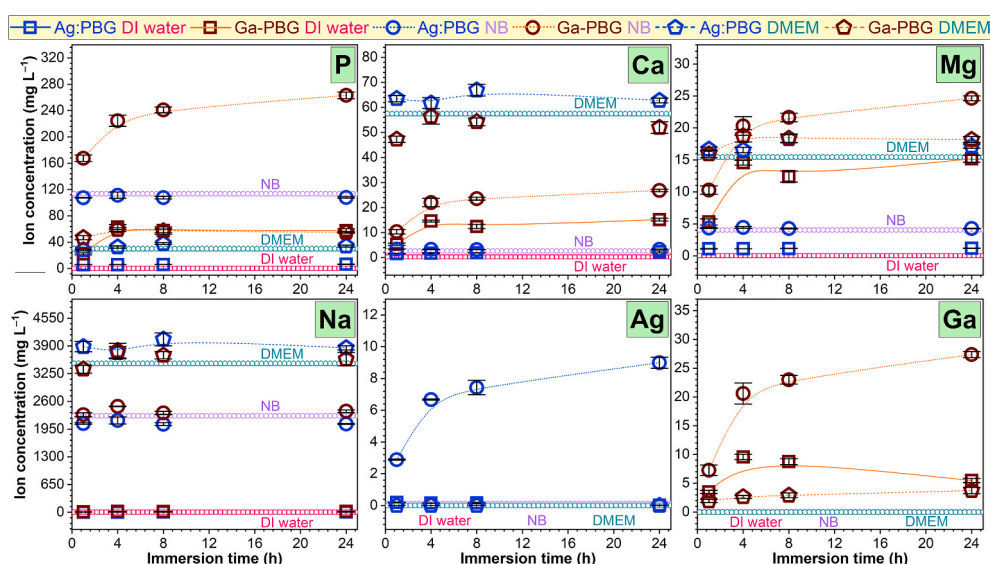

Fig. 8. P, Ca, Mg, Na, Ag and Ga ion release temporal profiles of Ag:PBG-PVD and Ga-PBG-PVD implant-type coatings in samples in DI water, NB and DMEM.

to have a "delivery on demand" therapeutic ion system, when the antibiotics become overwhelmed by bacteria proliferation, could prove of great interest for healthcare.

3.2.2. In vitro cytocompatibility assays

Human fibroblast (Hs27) and mesenchymal stem (hMSC) cells were cultured for 24 h on uncoated cp-Ti and cp-Ti coated with Ag:PBG-PVD and Ga-PBG-PVD-based layers to assess cytocompatibility. Due the opaque nature of the studied specimens, the cell morphology was observed by fluorescent microscopy. Cell proliferation (for both Hs27 and hMSC) and cell death (for Hs27) were assessed by MTS and LDH tests, respectively.

The morphology of the cells grown on PBG implant-type coatings presented all the hallmarks of a healthy cytoskeleton and nuclei. Hs27 cells were well-spread on all PBG coating surfaces and retained the characteristic morphology of their actin cytoskeleton (Fig. 9A–D). The nuclei were normal, without shape, dimension and genetic material condensation anomalies. Lack of micronuclei were noticed.

The MTS tests suggested that Hs27 presented cellular proliferation upon all Ag and Ga containing PBG coatings (Fig. 9E). Cells proliferated with 100% (polycarbonate control, Ga-PBG-PVD≈400 nm and Ga-PBG-PVD≈1400 nm), 85% (uncoated cp-Ti) and 56% (Ag:PBG-PVD) compared to the number of seeded cells. Statistical analysis indicated significant differences ($p < 0.05$, one-way Anova followed by Tukey Kramer's post hoc test) between polycarbonate control *vs.* cp-Ti control, both controls *vs.* Ag:PBG-PVD, and Ag:PBG-PVD *vs.* Ga-PBG-PVD layers.

No cytotoxic effects of any Ag or Ga containing PBG coatings were observed as a consequence of the ionic release of Na, Ca, P, Mg, Fe and Ag/Ga ions, relative to the controls (polycarbonate and cp-Ti) (Fig. 9F).

The Ag:PBG-PVD layers did however lead to a lower cell proliferation rate with respect to control, yet did not provoke cell death. While assessing the activity of lactate dehydrogenase (LDH), a noteworthy effect was signalled. Specifically, the Ga-PBG-PVD films elicit lower values than the blank leading to the conclusion that Ga ions released into the testing solution caused a degree of inhibition of this specific enzyme.

The hMSCs grown on PBG implant-type coatings presented a morphology typical for the cell line. The hMSCs retained their shape, were well-spread on the sample surfaces, having healthy lamellipodia and filopodia, and a normal distribution of actin microfilaments in the cytoskeleton (Fig. 10A–C). Only rare cells undergoing division were rounded. The nuclei had typical ovoid shape, with normal dimension and condensation of chromatin. No micronuclei were observed. The MTS tests suggested cellular proliferation on both Ag and Ga containing PBG layers (Fig. 10D). However, a delayed hMSCs proliferation was noticed for the Ag:PBG-PVD when compared to the bare cp-Ti and Ga-PBG-PVD≈1400 nm, similar to the Hs27 cells.

Overall, the morphological analysis of cells grown on these layers in conjunction with the cell proliferation data showed that these films were cytocompatible. Regarding the potential toxicity of the antimicrobial agents (Ag and Ga) in some systems (*e.g.*, nephrotoxicity, haemotoxicity), it should be highlighted that the PBG films leach a very small amount of Ag and Ga in total. Even in the event of total dissolution of the films, the amount of Ga released for a dental fixture (typically 3.75 mm thick and 11 mm long) covered with ≈1400 nm and ≈400 nm of Ga-PBG-PVD film would be approximately 200000–700000 times less than the Ga amount in the case of a course of Ga nitrate treatment for hypercalcemia [98–100] that has been shown to be a major risk in causing renal function impairment.
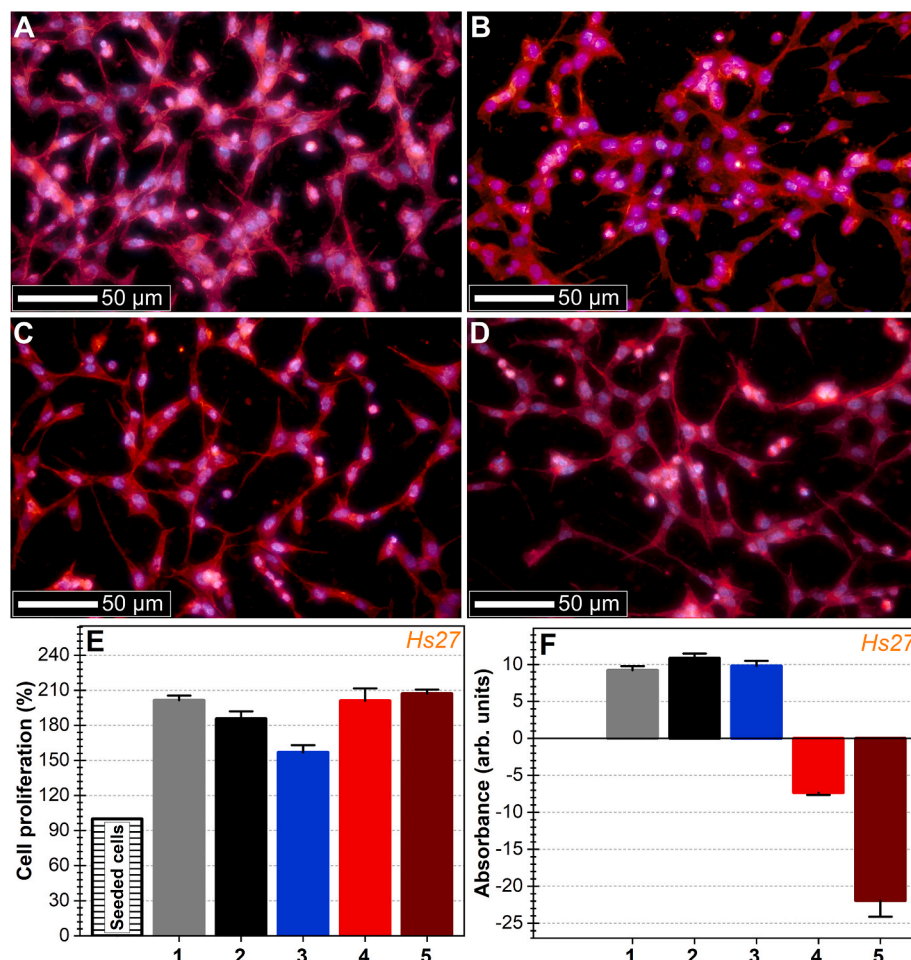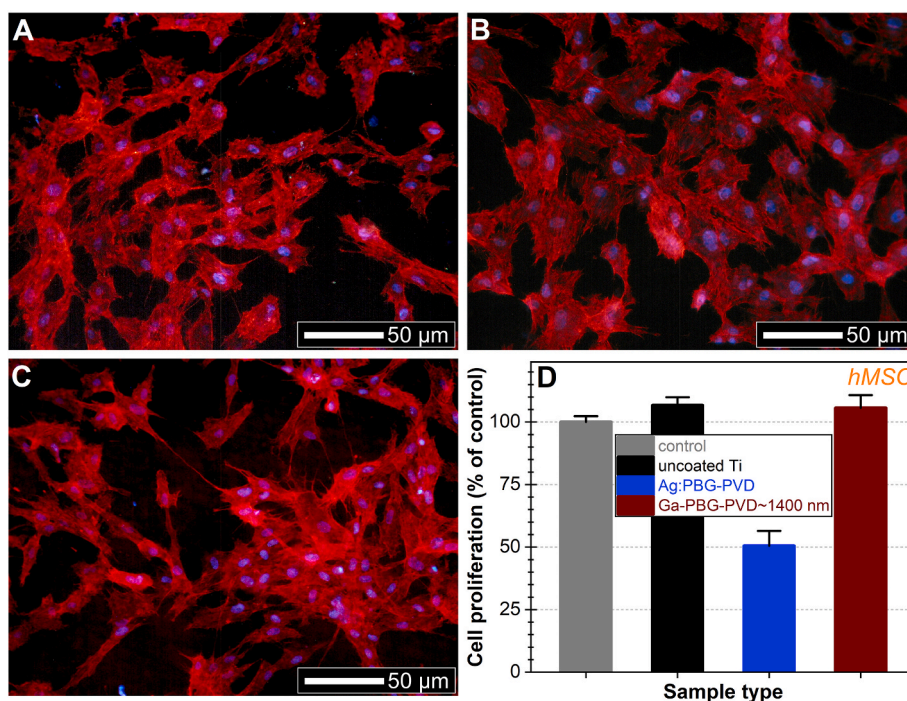

Fig. 9. (**A – D**) Morphology of Hs27 cells grown for 24 h on (**A**) uncoated cp-Ti and (**B**) Ag:PBG-PVD, (**C**) Ga-PBG-PVD≈400 nm and (**D**) Ga-PBG-PVD≈1400 nm coated cp-Ti. Actin microfilaments of the cell cytoskeleton were stained with phalloidin-AlexaFluor596 (red), whilst the cell nuclei were counterstained with DAPI (blue). (Bar charts) depicting the (**E**) cell proliferation and (**F**) cell toxicity at 24 h, obtained by MTS assay (values are normalized as percentages relative to the seeding cell number) and LDH assay (the values are shown in arbitrary absorption units), respectively for: (1) polycarbonate biological control, (2) Uncoated cp-Ti and (3) Ag:PBG-PVD, (4) Ga-PBG-PVD≈400 nm and (5) Ga-PBG-PVD≈1400 nm coated cp-Ti. (For interpretation of the references to colour in this figure legend, the reader is referred to the Web version of this article.)

Fig. 10. (**A – D**) Morphology of hMSC cells grown for 24 h on the (**A**) uncoated and (**B**) Ag:PBG-PVD and (**C**) Ga-PBG-PVD≈1400 nm coated cp-Ti. Actin microfilaments of the cell cytoskeleton were stained with phalloidin-AlexaFluor596 (red), whilst the cell nuclei were counterstained with DAPI (blue). (**D**) hMSC proliferation at 24 h, as assessed by a MTS test. (For interpretation of the references to colour in this figure legend, the reader is referred to the Web version of this article.)

3.2.3. Antibacterial activity tests

The antimicrobial efficacy of Ag:PBG and Ga-PBG PVD layers was assessed by quantification of viable colony forming units (CFU) after 6 and 24 h of culture with *S. aureus* (Fig. 11A) and *E. coli* (Fig. 11B). When culturing on the uncoated substrate, a progressive proliferation of bacteria (up to 3-log increase at 24 h) was observed, irrespective strain type.

The bactericidal effect of Ag:PBG and Ga-PBG layers was evidenced for both Gram-positive and Gram-negative bacteria. Similar antimicrobial trends were shown at both time points for all variants of PVD films in relation to Gram-negative *E. coli* where CFUs were reduced by 2 log (after 6 h) and 2.5 log (after 24 h) with respect to the initially seeded CFUs. In comparison to the uncoated substrate, a 3.5-log and 5-log *E. coli* reduction was recorded at 6 and 24 h, respectively. In the case of Gram-positive *S. aureus*, the antibacterial efficacy increased in the order Ag: PBG-PVD < Ga-PBG-PVD≈400 nm < Ga-PBG-PVD≈1400 nm, at all-time points. The proliferation of *S. aureus* was drastically reduced for the Ga-containing coatings, whereby a 5 and 6 log-reduction was recorded after 24 h in the case of Ga-PBG-PVD≈400 nm and Ga-PBG-PVD≈1400 nm, respectively, with respect to the uncoated substrate. The result suggests that the intensity of the effect can be controlled by varying the Ga-PBG-PVD film thickness (and thereby, the amount of therapeutic ions to be released).

If Ga has not been yet incorporated into calcium phosphates or bioactive glasses, a comparison on the antimicrobial effect of Ag particles of similar sizes (as employed in this study) can be attempted (even though it should be mentioned that the testing methods vary). Kirmanidou et al. [101] investigated the acceptable cytocompatible and antibacterial size range of Ag NPs applied to Ti6Al4V by electrochemical deposition to distribute particles ranging from 5 to 30 nm. They concluded that the 5–30 nm NPs had a pronounced antibacterial efficacy (at 24 h) with respect to *Porphyromonas gingivalis* and *Prevotella intermedia* strains (inferred by a serial dilution spotting assay), while only the 5 nm NPs induced a concentration-dependent decrease in bone osteosarcoma (Saos-2) cell proliferation rates at 48 h, followed by recovery at 72 h. Furthermore, Surmeneva et al. [102] produced a tri-layer system –

a 1.5 µg/cm^2 dispersion of electrophoretic deposited Ag NPs with sizes of 70 ± 20 nm, sandwiched between two magnetron sputtered calcium phosphate-based coatings – and suggested antibacterial efficacy against *E. coli* (following a semi-quantitative turbidity test) subsequent to a 1/3 release of Ag NPs over a 3-day period in Phosphate Buffered Saline solution. The structure presented a good cytocompatible response in human bone osteosarcoma (MG-63) cell cultures. By utilising the photosensitivity of Ag to light, Range et al. [103] incorporated up to 1.8 wt% of either Ag$^+$ or elemental Ag^0 (in dark or ambient light conditions, respectively) into calcium phosphate ceramics and compared their antibacterial properties against *E. coli* to Ag$_3$PO$_4$. A silver loading of ~0.89 wt% in the calcium phosphate coating, led to a 20 µg over time release in water, leading to the formation of inhibition zones similarly to Ag$_3$PO$_4$, which is indicative of an antibacterial effect. Satisfactory cytocompatibility in human epithelial cervical cancer (HeLa) cell cultures (unlike the case of Ag$_3$PO$_4$) was obtained. Chernozem et al. [104] manufactured intricate structures by the coating of TiO$_2$ nanotubes with electrophoretic deposited hybrid composites consisting of Ag and calcium phosphate NPs, which showed a promising antibacterial efficacy against *S. aureus*.

The antimicrobial effects of both Ag and Ga are dose dependent [34, 105]. Two mechanisms for Ag NPs mechanisms are possible, as reviewed elsewhere [105–107]: (*i*) direct contact (leading to the damage of bacterial cell membrane, and leakage of cell contents), enhanced for nanoparticles with sizes lower than 10 nm [106]; and (*ii*) by ion-release (upon penetration into the cytoplasm of cells, the ions will interact with proteins, lipids, and DNA, or by generating reactive oxygen species which can damage proteins and nucleic acids [105,107]. Ga^{3+} has significant potential as an effective antimicrobial element, due to what is currently referred as a the "Trojan horse" effect, by disrupting the ion metabolism of bacteria [34,50,108]. Ga^{3+} enters the bacteria by disguise through Fe^{3+} uptake systems, being masked via similar trivalency and ionic radius. Iron is part of many cellular enzymes, and is beneficial to the cell for its ability to change redox state, between 2+ and 3+. Iron is found as well in many intracellular bacterial enzymes and is involved in
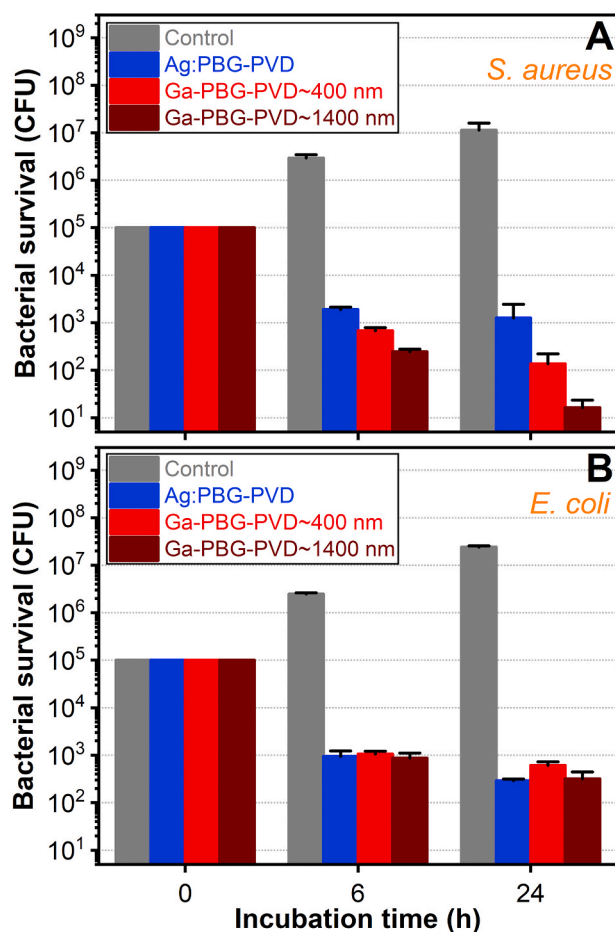
Fig. 11. Time evolution of the antibacterial activity of the Ag:PBG-PVD and Ga-PBG-PVD implant-type coatings against (**A**) *S. aureus* and (**B**) *E. coli*. The data are represented as logarithmic values of CFU mL^{-1} of bacterial cells.

crucial mechanisms such as DNA synthesis or cell metabolism (cytochromes, catalases, peroxidases). In contrast Ga^{3+} cannot be reduced to 2+ leading to detrimental cellular uptake of Ga over Fe.

As seen in the data presented above, Ga ions affect the activity of LDH in human cells, an enzyme involved in the energy generation by anaerobic glycolysis, NAD (nicotinamide adenine dinucleotide) system interaction that can transfer and deal with H$^-$ (hydride) ions being linked with the reactive oxygen species equilibrium). The LDH enzyme, found in both *S. aureus* and *E. coli* [109,110], could be disrupted along with many cellular processes that overwhelms the bacteria ability to repair and survive, thus resulting in an important bactericidal effect.

In the human blood, iron is found in concentrations ranging from 0.6 to 1.7 mg/L^{-1} circulating complexed with transferrin, an iron transporting protein. Thus, even the smallest Ga released concentration at 24 h (*i.e.*, 3.7 mg/L^{-1}, as tested in DMEM), is 10–100 fold larger than the free iron content found in blood. Therefore, the Ga ions can competitively enter the bacterial cells and replace iron in key enzymes. The smaller impact observed in Gram negative bacteria can be attributed to their more complex wall, which slows down the Ga ion penetration and redundant efflux mechanisms that overall lead to a lower intracellular Ga concentration.

Furthermore, in previous studies, Stuart et al. [14,26] demonstrated controlled ionic release rates of all constituents within PBG thin films until the point of complete dissolution. The continuous shedding of the surface may be an additional factor preventing bacterial attachment. Therefore, PBG films have the capacity to combat both initial attachment and subsequent biofilm formation onto medical implants, ranging from dental fixtures to hip stems.

Due to the tailor-ability of these coatings the quantity of therapeutic ions released in the body from such a new generation of implant coatings, can be controlled to be maintained at values 1000 times lower than where cytotoxic effects would appear.

By collective assessment of *in vitro* cytocompatibility and antibacterial testing, the results suggested that the Ga-PBG-PVD layers conferred superior bio-functionality to the implant-type surfaces. Furthermore, Ga^{3+} has demonstrated therapeutic effects on osteogenic cells, preventing bone resorption through inhibition of osteoclast activity and stimulation of osteoblasts [111]. Moreover, osteogenic ions such as Ca, P and Mg may eventually lead to enhanced proliferation and stimulation of pre-osteoblastic cells [112]. The controlled dissolution will allow for a time limiting layer to fight infection prior to revealing a sub-osteogenic layer such as hydroxyapatite or bioactive silicate glass. Thus, based on the presented information, we suggest for that Ga-PBG-PVD films are a promising and safe solution for the future development of advanced medical implants. Whilst encouraging here, further testing is still necessary in order to prove their complete suitability (when coupled with osteogenic layers).

4. Conclusions

Active agents of Ag and Ga were incorporated into PBG thin-film matrices to control the release of antimicrobial (Ga, Ag) and osteogenic (Ca, P, Mg) elements for application in next generation implant coatings. As such, a novel methodology, labelled here as "dual target consecutive co-sputtering", was shown by the TEM and XPS to successfully form 5 nm Ag clusters contained within a 46 nm thick PBG coating layer onto commercially pure Ti. Thereby, this advanced deposition variation showed good promise, and can be extended to foster fabrication of other metal-glass composites in biomedicine, but not limited to it, with potential utilization spanning to electronic thin film applications. On the other hand, Ga is reported to be effective in its ionic, Ga^{3+} form, and therefore a conventional approach of sputtering from a PBG containing Ga$_2$O$_3$ as a network modifier was employed to deposit 400 and 1400 nm thick coating layers.

Dissolution and ICP-MS ion release profiles were obtained over a 24 h period in various media [Dulbecco's Modified Eagle's Medium (DMEM), nutrient broth (NB), and deionized (DI) water] and highlighted a critical point for academic and industry wide investigation of standardised ISO methods, whereby a well-known disparity exists between dissolution behaviour in the wide variety of available *in vitro* media used. Shown here, Ag ions were released solely in NB (commonly used in antibacterial assays such as ISO 22196:2011) to maximum amounts of 9 ppm, whilst in DMEM (medium used for cytocompatibility assays, as outlined by ISO 10993-5:2009), no ionic release of Ag was identified (possibly being below the sensitivity limit). The ability to dissolve Ag nano-particles was attributed to the combined of presence chloride ions and the inadequate buffering ability of NB as compared to DMEM. The 1400 nm Ga containing coating showed at 24 h active Ga release of 6, 27, and 4 ppm in the DI water, NB and DMEM media, respectively. The PBG dissolution and therapeutic ions release seems to be linked to pH balancing capability, and thereby, a thorough study should be carried out in the near future, prior to the next phase of *in vivo* testing. The superior pH balancing activity of the intercellular environment might cause a reduced initial antimicrobial performance. However, one should also note that upon bacteria proliferation the local tissue environment changes dramatically, due to inflammation and leucocytes action, as a consequence causing a decrease in the pH balancing capacity of *in vivo* medium. Such conditions begin to be similar to ones met in the case of bacteria grown in nutrient broth, which is created to give such microorganisms the best chance for development.

To exemplify the functionality, both types of coating were tested for cytocompatibility (in human fibroblast – *Hs27* – and mesenchymal stem – *hMSC* – cells) and antibacterial efficacy (against *S. aureus* and *E. coli* strains) at 24 h. All Ag:PBG and Ga-PBG PVD samples were

cytocompatible, although signs of delayed (Hs27)/hindered (hMSC) cell proliferation were recorded in the case of Ag:PBG-PVD≈46 nm thin films with respect to the bare Ti control, whilst even in the case of the thicker (≈1400 nm) Ga-PBG-PVD coatings, no such events were noticed. Therefore, it is suggested that the use of much thicker Ag:PBG-PVD films could be suboptimal, whilst thicker Ga-PVD-PBG coatings could be further (and perhaps, safely) explored. Antibacterial efficacy at 24 h as assessed by measurement of CFUs showed promise relative to both Gram positive (*S. aureus*) (6-log reduction for Ga-PBG-PVD≈1400 nm, 5-log reduction for Ga-PBG-PVD≈400 nm and 4-log reduction for Ag:PBG-PVD≈46 nm) bacterial strains and Gram negative (*E. coli*) (5-log reduction for all PVD coatings) with respect to the uncoated Ti.

Thereby, the combined preliminary cytocompatibility – antimicrobial studies showed that both coating solutions have the potential to be used as sacrificial layers to counteract implant infection due to surface contamination. The results within this study could contribute to paving the way for the development of fully tailorable therapeutic films with widespread applicability in next generation endo-osseous implants such as hip stems or dental implants. Our future research studies will continue on the basis of these established premises.

CRediT authorship contribution statement

B.W. Stuart: Conceptualization, Methodology, Investigation, Writing – original draft, Writing – review & editing. **G.E. Stan:** Conceptualization, Methodology, Investigation, Writing – original draft, Writing – review & editing, Resources, Supervision. **A.C. Popa:** Methodology, Investigation. **M.J. Carrington:** Investigation, Writing – review & editing. **I. Zgura:** Methodology, Investigation. **M. Necsulescu:** Methodology, Investigation. **D.M. Grant:** Writing – review & editing, Resources, Supervision, Funding acquisition.

Declaration of competing interest

The authors declare that they have no known competing financial interests or personal relationships that could have appeared to influence the work reported in this paper.

Acknowledgements

References

[1] World Health Organization, Antimicrobial resistance. https://www.who.int/news-room/fact-sheets/detail/antimicrobial-resistance, 2018. April 17, 2021.

[2] B. Li, T.J. Webster, Bacteria antibiotic resistance: new challenges and opportunities for implant-associated orthopedic infections, J. Orthop. Res. 36 (2018) 22–32, https://doi.org/10.1002/jor.23656.

[3] A.C. Popa, H.R. Fernandes, M. Necsulescu, C. Luculescu, M. Cioangher, V. Dumitru, B.W. Stuart, D.M. Grant, J.M.F. Ferreira, G.E. Stan, Antibacterial efficiency of alkali-free bio-glasses incorporating ZnO and/or SrO as therapeutic agents, Ceram. Int. 45 (2019) 4368–4380, https://doi.org/10.1016/j.ceramint.2018.11.112.

[4] 17th Annual Report, National joint Registry for England, Wales, Northern Ireland and the Isle of Man, 2020, pp. 1–312. https://reports.njrcentre.org.uk/Portals/0/PDFdownloads/NJR 17th Annual Report 2020.pdf. (Accessed 17 April 2021).

[5] S. Awasthi, S.K. Pandey, E. Arunan, C. Srivastava, A review on hydroxyapatite coatings for the biomedical applications: experimental and theoretical perspectives, J. Mater. Chem. B 9 (2021) 228–249, https://doi.org/10.1039/D0TB02407D.

[6] L. Drago, M. Toscano, M. Bottagisio, Recent evidence on bioactive glass antimicrobial and antibiofilm activity: a mini-review, Materials 11 (2018) 326, https://doi.org/10.3390/ma11020326.

[7] R.A. Surmenev, M.A. Surmeneva, A.A. Ivanova, Significance of calcium phosphate coatings for the enhancement of new bone osteogenesis – a review, Acta Biomater. 10 (2014) 557–579, https://doi.org/10.1016/j.actbio.2013.10.036.

[8] M. Epple, Review of potential health risks associated with nanoscopic calcium phosphate, Acta Biomater. 77 (2018) 1–14, https://doi.org/10.1016/j.actbio.2018.07.036.

[9] D.S. Brauer, Phosphate glasses, in: J.R. Jones, A.G. Clare (Eds.), Bio-Glasses: an Introduction, John Wiley & Sons, Hoboken, 2012, pp. 45–64.

[10] J. Henao, C. Poblano-Salas, M. Monsalve, J. Corona-Castuera, O. Barceinas-Sanchez, Bio-active glass coatings manufactured by thermal spray: a status report, J. Mater. Res. Technol 8 (2019) 4965–4984, https://doi.org/10.1016/j.jmrt.2019.07.011.

[11] R. Sergi, D. Bellucci, V. Cannillo, A comprehensive review of bioactive glass coatings: state of the art, challenges and future perspectives, Coatings 10 (2020) 757, https://doi.org/10.3390/coatings10080757.

[12] R.D. Bloebaum, D. Beeks, L.D. Dorr, C.G. Savory, J.A. DuPont, A.A. Hofmann, Complications with hydroxyapatite particulate separation in total hip arthroplasty, Clin. Orthop. Relat. Res. 298 (1994) 19–26, https://doi.org/10.1097/00003086-199401000-00005.

[13] B. Li, X. Xia, M. Guo, Y. Jiang, Y. Li, Z. Zhang, S. Liu, H. Li, C. Liang, H. Wang, Biological and antibacterial properties of the micro-nanostructured hydroxyapatite/chitosan coating on titanium, Sci. Rep. 9 (2019) 14052, https://doi.org/10.1038/s41598-019-49941-0.

[14] B.W. Stuart, M. Gimeno-Fabra, J. Segal, I. Ahmed, D.M. Grant, Degradation and characterization of resorbable phosphate-based glass thin-film coatings applied by radio-frequency magnetron sputtering, ACS Appl. Mater. Interfaces 7 (2015) 27362–27372, https://doi.org/10.1021/acsami.5b08957.

[15] J. Ballarre, T. Aydemir, L. Liverani, J.A. Roether, W.H. Goldmann, A. R. Boccaccini, Versatile bioactive and antibacterial coating system based on silica, gentamicin, and chitosan: improving early stage performance of titanium implants, Surf. Coating. Technol. 381 (2020), 125138, https://doi.org/10.1016/j.surfcoat.2019.125138.

[16] A. Kulkarni Aranya, S. Pushalkar, M. Zhao, R.Z. LeGeros, Y. Zhang, D. Saxena, Antibacterial and bioactive coatings on titanium implant surfaces, J. Biomed. Mater. Res. 105 (2017) 2218–2227, https://doi.org/10.1002/jbm.a.36081.

[17] E.L. Cyphert, H.A. von Recum, Emerging technologies for long-term antimicrobial device coatings: advantages and limitations, Exp. Biol. Med. 242 (2017) 788–798, https://doi.org/10.1177/1535370216688572.

[18] T. Tite, A.C. Popa, L.M. Balescu, I.M. Bogdan, I. Pasuk, J.M.F. Ferreira, G.E. Stan, Cationic substitutions in hydroxyapatite: current status of the derived biofunctional effects and their in vitro interrogation methods, Materials 11 (2018) 2081, https://doi.org/10.3390/ma11112081.

[19] L. Ramos Rivera, A. Cochis, S. Bisera, E. Canciani, S. Ferraris, L. Rimondini, A. R. Boccaccini, Antibacterial, pro-angiogenic and pro-osteointegrative zein-bioactive glass/copper based coatings for implantable stainless steel aimed at bone healing, Bioactive Mater 6 (2021) 1479–1490, https://doi.org/10.1016/j.bioactmat.2020.11.001.

[20] L.D. Soule, N. Pajares Chomorro, K. Chuong, N. Mellott, N. Hammer, K. D. Hankenson, X. Chatzistavrou, Sol–Gel-derived bioactive and antibacterial multi-component thin films by the spin-coating technique, ACS Biomater. Sci. Eng. 6 (2020) 5549–5562, https://doi.org/10.1021/acsbiomaterials.0c01140.

[21] A.A. Ivanova, M.A. Surmeneva, A.I. Tyurin, T.S. Pirozhkova, I.A. Shuvarin, O. Prymak, M. Epple, M.V. Chaikina, R.A. Surmenev, Fabrication and physico-mechanical properties of thin magnetron sputter deposited silver-containing hydroxyapatite films, Appl. Surf. Sci. 360 (2016) 929–935, https://doi.org/10.1016/j.apsusc.2015.11.087. Part B.

[22] G. Popescu-Pelin, C. Ristoscu, L. Duta, G.E. Stan, I. Pasuk, T. Tite, M.S. Stan, C. Bleotu, M. Popa, M.C. Chifiriuc, F.N. Oktar, A. Nicarel, I.N. Mihailescu, Antimicrobial and cytocompatible bovine hydroxyapatite-alumina-zeolite composite coatings synthesized by pulsed laser deposition from low-cost sustainable natural resources, ACS Sustain. Chem. Eng. 8 (2020) 4026–4036, https://doi.org/10.1021/acssuschemeng.9b05031.

[23] M.T. Islam, R.M. Felfel, E.A. Abou Neel, D.M. Grant, I. Ahmed, K.M.Z. Hossain, Bioactive calcium phosphate–based glasses and ceramics and their biomedical applications: a review, J. Tissue Eng. 8 (2017), https://doi.org/10.1177/2041731417719170, 2041731417719170.

[24] N.J. Lakhkar, I.H. Lee, H.W. Kim, V. Salih, I.B. Wall, J.C. Knowles, Bone formation controlled by biologically relevant inorganic ions: role and controlled delivery from phosphate-based glasses, Adv. Drug Deliv. Rev. 65 (2013) 405–420, https://doi.org/10.1016/j.addr.2012.05.015.

[25] M. Al Qaysi, A. Petrie, R. Shah, J.C. Knowles, Degradation of zinc containing phosphate-based glass as a material for orthopedic tissue engineering, J. Mater. Sci. Mater. Med. 27 (2016) 157, https://doi.org/10.1007/s10856-016-5770-x.

[26] B.W. Stuart, M. Gimeno-Fabra, J. Segal, I. Ahmed, D.M. Grant, Mechanical, structural and dissolution properties of heat treated thin-film phosphate based glasses, Appl. Surf. Sci. 416 (2017) 605–617, https://doi.org/10.1016/j.apsusc.2017.04.110.

[27] E. Mohseni, E. Zalnezhad, A.R. Bushroa, Comparative investigation on the adhesion of hydroxyapatite coating on Ti-6Al-4V implant: a review paper, Int. J. Adhesion Adhes. 48 (2014) 238–257, https://doi.org/10.1016/j.ijadhadh.2013.09.030.

[28] A. Frei, Metal complexes, an untapped source of antibiotic potential? Antibiotics 9 (2020) 90, https://doi.org/10.3390/antibiotics9020090.

[29] J.R. Morones-Ramirez, J.A. Winkler, C.S. Spina, J.J. Collins, Silver enhances antibiotic activity against gram-negative bacteria, Sci. Transl. Med. 5 (2013), 190ra81, https://doi.org/10.1126/scitranslmed.3006276.

[30] A.B.G. Lansdown, Silver in health care: antimicrobial effects and safety in use, Curr. Probl. Dermatol. 33 (2006) 17–34, https://doi.org/10.1159/000093928.

[31] N. Hadrup, A.K. Sharma, K. Loeschner, Toxicity of silver ions, metallic silver, and silver nanoparticle materials after in vivo dermal and mucosal surface exposure: a review, Regul. Toxicol. Pharmacol. 98 (2018) 257–267, https://doi.org/10.1016/j.yrtph.2018.08.007.

[32] S. Crunkhorn, Gallium fights infection in phase I trial, Nat. Rev. Drug Discov. 17 (2018) 786, https://doi.org/10.1038/nrd.2018.186.

[33] S. Hijazi, D. Visaggio, M. Pirolo, E. Frangipani, L. Bernstein, P. Visca, Antimicrobial activity of gallium compounds on ESKAPE pathogens, Front. Cell. Infect. Microbiol. 8 (2018) 316, https://doi.org/10.3389/fcimb.2018.00316.

[34] C.H. Goss, Y. Kaneko, L. Khuu, G.D. Anderson, S. Ravishankar, M.L. Aitken, N. Lechtzin, G. Zhou, D.M. Czyz, K. McLean, O. Olakanmi, H.A. Shuman, M. Teresi, E. Wilhelm, E. Caldwell, S.J. Salipante, D.B. Hornick, R.J. Siehnel, L. Becker, B.E. Britigan, P.K. Singh, Gallium disrupts bacterial iron metabolism and has therapeutic effects in mice and humans with lung infections, Sci. Transl. Med. 10 (2018), eaat7520, https://doi.org/10.1126/scitranslmed.aat7520.

[35] L.C.S. Antunes, F. Imperi, F. Minandri, P. Visca, In vitro and in vivo antimicrobial activities of gallium nitrate against multidrug-resistant Acinetobacter baumannii, Antimicrob. Agents Chemother. 56 (2012) 5961–5970, https://doi.org/10.1128/AAC.01519-12.

[36] F. Minandri, C. Bonchi, E. Frangipani, F. Imperi, P. Visca, Promises and failures of gallium as an antibacterial agent, Future Microbiol. 9 (2014) 379–397, https://doi.org/10.2217/fmb.14.3.

[37] I. Ahmed, E.A. Abou Neel, S.P. Valappil, S.N. Nazhat, D.M. Pickup, D. Carta, D. L. Carroll, R.J. Newport, M.E. Smith, J.C. Knowles, The structure and properties of silver-doped phosphate-based glasses, J. Mater. Sci. 42 (2007) 9827–9835, https://doi.org/10.1007/s10853-007-2008-9.

[38] S. Lee, T. Nakano, T. Kasuga, Structure, dissolution behavior, cytocompatibility, and antibacterial activity of silver-containing calcium phosphate invert glasses, J. Biomed. Mater. Res. 105 (2017) 3127–3135, https://doi.org/10.1002/jbm.a.36173.

[39] B.A. Kyffin, F. Foroutan, S.E. Taylor, D. Carta, F.N.S. Raja, R.A. Martin, D. M. Pickup, Antibacterial silver-doped phosphate-based glasses prepared by coacervation, J. Mater. Chem. B. 7 (2019) 7744–7755, https://doi.org/10.1039/c9tb02195g.

[40] S.P. Valappil, D. Ready, E.A. Abou Neel, D.M. Pickup, L.A. O'Dell, W. Chrzanowski, J. Pratten, R.J. Newport, M.E. Smith, M. Wilson, J.C. Knowles, Controlled delivery of antimicrobial gallium ions from phosphate-based glasses, Acta Biomater. 5 (2009) 1198–1210, https://doi.org/10.1016/j.actbio.2008.09.019.

[41] A. Łapa, M. Cresswell, I. Campbell, P. Jackson, W.H. Goldmann, R. Detsch, A. R. Boccaccini, Gallium- and Cerium-doped phosphate glasses with antibacterial properties for medical applications, Adv. Eng. Mater. 22 (2020), 1901577, https://doi.org/10.1002/adem.201901577.

[42] K. Wasa, I. Kanno, H. Kotera, Handbook of Sputter Deposition Technology: Fundamentals and Applications for Functional Thin Films, in: Nano-Materials and MEMS, second ed., Elsevier, 2012, pp. 1–644, https://doi.org/10.1016/C2010-0-67037-4.

[43] C. Besleaga, V. Dumitru, L.M. Trinca, A.C. Popa, C.C. Negrila, Ł. Kołodziejczyk, C. R. Luculescu, G.C. Ionescu, R.G. Ripeanu, A. Vladescu, G.E. Stan, Mechanical, corrosion and biological properties of room-temperature sputtered aluminum nitride films with dissimilar nanostructure, Nanomaterials 7 (2017) 394, https://doi.org/10.3390/nano7110394.

[44] G.E. Stan, A.C. Popescu, I.N. Mihailescu, D.A. Marcov, R.C. Mustata, L.E. Sima, S. M. Petrescu, A. Ianculescu, R. Trusca, C.O. Morosanu, On the bioactivity of adherent bioglass thin films synthesized by magnetron sputtering techniques, Thin Solid Films 518 (2010) 5955–5964, https://doi.org/10.1016/j.tsf.2010.05.104.

[45] A.C. Popa, V.M.F. Marques, G.E. Stan, M.A. Husanu, A.C. Galca, C. Ghica, D. U. Tulyaganov, A.F. Lemos, J.M.F. Ferreira, Nanomechanical characterization of bioglass films synthesized by magnetron sputtering, Thin Solid Films 553 (2014) 166–172, https://doi.org/10.1016/j.tsf.2013.10.104.

[46] B.W. Stuart, J.J. Titman, M. Gimeno-Fabra, I. Ahmed, D.M. Grant, Insights into structural characterisation and thermal properties of compositionally equivalent vapour-condensed and melt-quenched glasses, Mater. Des. 111 (2016) 174–184, https://doi.org/10.1016/j.matdes.2016.08.063.

[47] T. Tite, A.C. Popa, B.W. Stuart, A.C. Galca, L.M. Balescu, G. Popescu-Pelin, D.M. Grant, J.M.F. Ferreira, G.E. Stan, Phosphate bioglass thin-films: cross-area uniformity, structure and biological performance tailored by the simple modification of magnetron sputtering gas pressure, Appl. Surf. Sci. 541 (2021), 148640, https://doi.org/10.1016/j.apsusc.2020.148640.

[48] B. Stuart, M. Gimeno-Fabra, J. Segal, I. Ahmed, D.M. Grant, Preferential sputtering in phosphate glass systems for the processing of bioactive coatings, Thin Solid Films 589 (2015) 534–542, https://doi.org/10.1016/j.tsf.2015.05.072.

[49] P.S. Sato, T. Watanabe, H. Maeda, A. Obata, T. Kasuga, Preparation of an antibacterial amorphous phosphate based film by radiofrequency magnetron sputtering using a 65ZnO–30P$_2$O$_5$–5Nb$_2$O$_5$ glass, J. Non-Cryst. Solids 528 (2020), 119724, https://doi.org/10.1016/j.jnoncrysol.2019.119724.

[50] B.W. Stuart, C.A. Grant, G.E. Stan, A.C. Popa, J.J. Titman, D.M. Grant, Gallium incorporation into phosphate based glasses: bulk and thin film properties, J. Mech. Behav. Biomed. Mater. 82 (2018) 371–382, https://doi.org/10.1016/j.jmbbm.2018.03.041.

[51] A.B.G. Lansdown, A pharmacological and toxicological profile of silver as an antimicrobial agent in medical devices, Adv. Pharmacol. Sci. (2010), 910686, https://doi.org/10.1155/2010/910686, 2010.

[52] F. Sambale, S. Wagner, F. Stahl, R.R. Khaydarov, T. Scheper, D. Bahnemann, Investigations of the toxic effect of silver nanoparticles on mammalian cell lines, J. Nanomater. (2015), 136765, https://doi.org/10.1155/2015/136765, 2015.

[53] https://www.who.int/water_sanitation_health/publications/silver-02032018.pdf. (Accessed 17 April 2021).

[54] S.B. Goodman, The effects of micromotion and particulate materials on tissue differentiation: bone chamber studies in rabbits, Acta Orthop. Scand. 65 (1994) 1–43, https://doi.org/10.3109/17453679409155227.

[55] G.E. Stan, T. Tite, A.-C. Popa, I.M. Chirica, C.C. Negrila, C. Besleaga, I. Zgura, A. C. Sergentu, G. Popescu-Pelin, D. Cristea, L.E. Ionescu, M. Necsulescu, H. R. Fernandes, J.M.F. Ferreira, The beneficial mechanical and biological outcomes of thin Copper-Gallium doped silica-rich bio-active glass implant-type coatings, Coatings 10 (2020) 1119, https://doi.org/10.3390/coatings10111119.

[56] D.K. Owens, R.C. Wendt, Estimation of the surface free energy of polymers, J. Appl. Polym. Sci. 13 (1969) 1741–1747, https://doi.org/10.1002/app.1969.070130815.

[57] International Organization for Standardization, ISO 10993-5:2009 - biological evaluation of medical devices. Part 5: tests for in vitro cytotoxicity, Geneva, Switzerland. https://www.iso.org/standard/36406.html, 2009.

[58] B. Alberts, A. Johnson, J. Lewis, M. Raff, K. Roberts, P. Walter, Molecular Biology of the Cell, fourth ed., Garland Science, New York, 2002.

[59] International Organization for Standardization, ISO 22196:2011 - measurement of antibacterial activity on plastics and other non-porous surfaces, Geneva, Switzerland. https://www.iso.org/standard/54431.html, 2011.

[60] C.E. Heim, D. Vidlak, T.D. Scherr, C.W. Hartman, K.L. Garvin, T. Kielian, IL-12 promotes myeloid-derived suppressor cell recruitment and bacterial persistence during Staphylococcus aureus orthopedic implant infection, J. Immunol. 194 (2015) 3861–3872, https://doi.org/10.4049/jimmunol.1402689.

[61] C.R. Arciola, D. Campoccia, L. Montanaro, Implant infections: adhesion, biofilm formation and immune evasion, Nat. Rev. Microbiol. 16 (2018) 397–409, https://doi.org/10.1038/s41579-018-0019-y.

[62] L. Montanaro, P. Speziale, D. Campoccia, S. Ravaioli, I. Cangini, G. Pietrocola, S. Giannini, C.R. Arciola, Scenery of Staphylococcus implant infections in orthopedics, Future Microbiol. 6 (2011) 1329–1349, https://doi.org/10.2217/fmb.11.117.

[63] A.D. Pye, D.E.A. Lockhart, M.P. Dawson, C.A. Murray, A.J. Smith, A review of dental implants and infection, J. Hosp. Infect. 72 (2009) 104–110, https://doi.org/10.1016/j.jhin.2009.02.010.

[64] W.F. Oliveira, P.M.S. Silva, R.C.S. Silva, G.M.M. Silva, G. Machado, L.C.B. B. Coelho, M.T.S. Correia, Staphylococcus aureus and Staphylococcus epidermidis infections on implants, J. Hosp. Infect. 98 (2018) 111–117, https://doi.org/10.1016/j.jhin.2017.11.008.

[65] Z. Khatoon, C.D. McTiernan, E.J. Suuronen, T.-F. Mah, E.I. Alarcon, Bacterial biofilm formation on implantable devices and approaches to its treatment and prevention, Heliyon 4 (2018), e01067, https://doi.org/10.1016/j.heliyon.2018.e01067.

[66] L. Crémet, A. Broquet, B. Brulin, C. Jacqueline, S. Dauvergne, R. Brion, K. Asehnoune, S. Corvec, D. Heymann, N. Caroff, Pathogenic potential of Escherichia coli clinical strains from orthopedic implant infections towards human osteoblastic cells, Pathog. Dis. 73 (2015), https://doi.org/10.1093/femspd/ftv065 ftv065.

[67] M.W. Hussain, S.S. Abullais, T.A. Naqash, M.Y.S. Bhat, Microbial etiology and antimicrobial therapy of peri-implantitis: a comprehensive review, Open Dent. J. 12 (2019) 1113–1122, https://doi.org/10.2174/1874210601812011113.

[68] A. Kiani, J.V. Hanna, S.P. King, G.J. Rees, M.E. Smith, N. Roohpour, V. Salih, J. C. Knowles, Structural characterization and physical properties of P$_2$O$_5$–CaO–Na$_2$O–TiO$_2$ glasses by Fourier transform infrared, Raman and solid-state magic angle spinning nuclear magnetic resonance spectroscopies, Acta Biomater. 8 (2012) 333–340, https://doi.org/10.1016/j.actbio.2011.08.025.

[69] G. Le Saoût, P. Simon, F. Fayon, A. Blin, Y. Vaills, Raman and infrared study of (PbO)$_x$(P$_2$O$_5$)$_{(1-x)}$ glasses, J. Raman Spectrosc. 33 (2002) 740–746, https://doi.org/10.1002/jrs.911.

[70] M. Emmerson, A microbiologist's view of factors contributing to infection, New Horiz 6 (1998). S3-10, http://www.ncbi.nlm.nih.gov/pubmed/9654307.

[71] K.A. Poelstra, N.A. Barekzi, A.M. Rediske, A.G. Felts, J.B. Slunt, D.W. Grainger, Prophylactic treatment of gram-positive and gram-negative abdominal implant infections using locally delivered polyclonal antibodies, J. Biomed. Mater. Res. 60 (2002) 206–215, https://doi.org/10.1002/jbm.10069.

[72] J.A. Thornton, The microstructure of sputter-deposited coatings, J. Vac. Sci. Technol., A 4 (1986) 3059, https://doi.org/10.1116/1.573628 (1986).

[73] S. Calderon Velasco, A. Cavaleiro, S. Carvalho, Functional properties of ceramic-Ag nanocomposite coatings produced by magnetron sputtering, Prog. Mater. Sci. 84 (2016) 158–191, https://doi.org/10.1016/j.pmatsci.2016.09.005.

[74] C.D. Wagner, Handbook of X-Ray Photoelectron Spectroscopy: A Reference Book of Standard Data for Use in X-Ray Photoelectron Spectroscopy, Physical Electronics Division, Perkin-Elmer Corporation, 1979.

[75] G. Schön, J. Tummavuori, B. Lindström, C.R. Enzell, C.R. Enzell, C.-G. Swahn, ESCA studies of Ag, Ag_2O and AgO, Acta Chem. Scand. 27 (1973) 2623–2633, https://doi.org/10.3891/acta.chem.scand.27-2623.

[76] V.K. Kaushik, XPS core level spectra and Auger parameters for some silver compounds, J. Electron. Spectrosc. Relat. Phenom. 56 (1991) 273–277, https://doi.org/10.1016/0368-2048(91)85008-H.

[77] Y. Liu, R.G. Jordan, S.L. Qiu, Electronic structures of ordered Ag-Mg alloys, Phys. Rev. B 49 (1994) 4478–4484, https://doi.org/10.1103/PhysRevB.49.4478.

[78] L.H. Tjeng, M.B.J. Meinders, J. Van Elp, J. Ghijsen, G.A. Sawatzky, R.L. Johnson, Electronic structure of Ag_2O, Phys. Rev. B 41 (1990) 3190–3199, https://doi.org/10.1103/PhysRevB.41.3190.

[79] G. Cossu, G.M. Ingo, G. Mattogno, G. Padeletti, G.M. Proietti, XPS investigation on vacuum thermal desorption of UV/ozone treated GaAs(100) surfaces, Appl. Surf. Sci. 56–58 (1992) 81–88, https://doi.org/10.1016/0169-4332(92)90219-N.

[80] G. Schön, Auger and direct electron spectra in X-ray photoelectron studies of zinc, zinc oxide, gallium and gallium oxide, J. Electron. Spectrosc. Relat. Phenom. 2 (1973) 75–86, https://doi.org/10.1016/0368-2048(73)80049-0.

[81] S. Evans, Energy calibration secondary standards for X-ray photoelectron spectrometers, Surf. Interface Anal. 7 (1985) 299–302, https://doi.org/10.1002/sia.740070609.

[82] M. Pelavin, D.N. Hendrickson, J.M. Hollander, W.L. Jolly, Phosphorus 2p electron binding energies. Correlation with extended Hückel charges, J. Phys. Chem. 74 (1970) 1116–1121, https://doi.org/10.1021/j100700a027.

[83] R. Franke, T. Chassé, P. Streubel, A. Meisel, Auger parameters and relaxation energies of phosphorus in solid compounds, J. Electron. Spectrosc. Relat. Phenom. 56 (1991) 381–388, https://doi.org/10.1016/0368-2048(91)85035-R.

[84] B.V.R. Chowdari, K.F. Mok, J.M. Xie, R. Gopalakrishnan, The influence of anion substitution on some phosphate-based ion conducting glasses, in: B.V. R. Chowdari, M. Yahaya, I.A. Talib, M.M. Salleh (Eds.), Solid State Ion. Mater., World Scientific Pubishing Co., Singapore, 1994, pp. 59–68, https://doi.org/10.1142/2448.

[85] V. Simon, D. Muresan, A.F. Takács, M. Neumann, S. Simon, Local order changes induced in calcium-sodium-phosphate glasses by transition metals, Solid State Ionics 178 (2007) 221–225, https://doi.org/10.1016/j.ssi.2006.12.011.

[86] A. Majjane, A. Chahine, M. Et-Tabirou, B. Echchahed, T.O. Do, P.M. Breen, X-ray photoelectron spectroscopy (XPS) and FTIR studies of vanadium barium phosphate glasses, Mater. Chem. Phys. 143 (2014) 779–787, https://doi.org/10.1016/j.matchemphys.2013.10.013.

[87] M. Crobu, A. Rossi, F. Mangolini, N.D. Spencer, Chain-length-identification strategy in zinc polyphosphate glasses by means of XPS and ToF-SIMS, Anal. Bioanal. Chem. 403 (2012) 1415–1432, https://doi.org/10.1007/s00216-012-5836-7.

[88] J. Drelich, E. Chibowski, Superhydrophilic and superwetting surfaces: definition and mechanisms of control, Langmuir 26 (2010) 18621–18623, https://doi.org/10.1021/la1039893.

[89] C.J. Wilson, R.E. Clegg, D.I. Leavesley, M.J. Pearcy, Mediation of biomaterial-cell interactions by adsorbed proteins: a review, Tissue Eng. 11 (2005) 1–18, https://doi.org/10.1089/ten.2005.11.1.

[90] A.C. Popa, G.E. Stan, M.A. Husanu, I. Mercioniu, L.F. Santos, H.R. Fernandes, J.M. F. Ferreira, Bioglass implant-coating interactions in synthetic physiological fluids with varying degrees of biomimicry, Int. J. Nanomed. 12 (2017) 683–707, https://doi.org/10.2147/IJN.S123236.

[91] A.V. Gayathri Devi, V. Rajendran, N. Rajendran, Structure, solubility and bioactivity in TiO_2-doped phosphate-based bioglasses and glass–ceramics, Mater. Chem. Phys. 124 (2010) 312–318, https://doi.org/10.1016/j.matchemphys.2010.06.038.

[92] T. Kokubo, H. Takadama, How useful is SBF in predicting in vivo bone bioactivity? Biomaterials 27 (2006) 2907–2915, https://doi.org/10.1016/j.biomaterials.2006.01.017.

[93] A. Cuneyt Tas, Grade-1 titanium soaked in a DMEM solution at 37 °C, Mater. Sci. Eng. C 36 (2014) 84–94, https://doi.org/10.1016/j.msec.2013.11.045.

[94] S. Lopez-Esteban, C.F. Gutierrez-Gonzalez, L. Gremillard, E. Saiz, A.P. Tomsia, Interfaces in graded coatings on titanium-based implants, J. Biomed. Mater. A 88 (2009) 1010–1021, https://doi.org/10.1002/jbm.a.31935.

[95] C.N. Carvalho, L.G. Freire, A.P.L. de Carvalho, M.A.H. Duarte, J. Bauer, G. Gavini, Ions release and pH of calcium hydroxide–, chlorhexidine– and bioactive glass–based endodontic medicaments, Braz. Dent. J. 27 (2016) 325–331, https://doi.org/10.1590/0103-6440201600602.

[96] E. Mancuso, O.A. Bretcanu, M. Marshall, M.A. Birch, A.W. McCaskie, K. W. Dalgarno, Novel bioglasses for bone tissue repair and regeneration: effect of glass design on sintering ability, ion release and biocompatibility, Mater. Des. 129 (2017) 239–248, https://doi.org/10.1016/j.matdes.2017.05.037.

[97] S.I. Schmitz, B. Widholz, C. Essers, M. Becker, D.U. Tulyaganov, A. Moghaddam, I. Gonzalo de Juan, F. Westhauser, Superior biocompatibility and comparable osteoinductive properties: sodium-reduced fluoride-containing bioactive glass belonging to the CaO–MgO–SiO_2 system as a promising alternative to 45S5 bioactive glass, Bioact. Mater. 5 (2020) 55–65, https://doi.org/10.1016/j.bioactmat.2019.12.005.

[98] C.R. Chitambar, Medical applications and toxicities of gallium compounds, Int. J. Environ. Res. Publ. Health 7 (2010) 2337–2361, https://doi.org/10.3390/ijerph7052337.

[99] R.P. Warrell, W.K. Murphy, P. Schulman, P.J. O'Dwyer, G. Heller, A randomized double-blind study of gallium nitrate compared with etidronate for acute control of cancer-related hypercalcemia, J. Clin. Oncol. 9 (1991) 1467–1475, https://doi.org/10.1200/JCO.1991.9.8.1467.

[100] N. Zojer, A.V. Keck, M. Pecherstorfer, Comparative tolerability of drug therapies for hypercalcaemia of malignancy, Drug Saf. 21 (1999) 389–406, https://doi.org/10.2165/00002018-199921050-00004.

[101] Y. Kirmanidou, M. Sidira, A. Bakopoulou, A. Tsouknidas, O. Prymak, R. Papid, T. Choli-Papadopoulou, M. Epple, N. Michailidis, P. Koidis, K. Michalakis, Assessment of cytotoxicity and antibacterial effects of silver nanoparticle-doped titanium alloy surfaces, Dent. Mater. 35 (2019) e220–e233, https://doi.org/10.1016/j.dental.2019.06.003.

[102] M.A. Surmeneva, A.A. Sharonova, S. Chernousova, O. Prymak, K. Loza, M. S. Tkachev, I.A. Shulepov, M. Epple, R.A. Surmenev, Incorporation of silver nanoparticles into magnetron-sputtered calcium phosphate layers on titanium as an antibacterial coating, Colloids Surf. B Biointerfaces 156 (2017) 104–113, https://doi.org/10.1016/j.colsurfb.2017.05.016.

[103] S. Range, D. Hagmeyer, O. Rotan, V. Sokolova, J. Verheyen, B. Siebers, M. Epple, A continuous method to prepare poorly crystalline silver-doped calcium phosphate ceramics with antibacterial properties, RSC Adv. 5 (2015) 43172–43177, https://doi.org/10.1039/C5RA00401B.

[104] R.V. Chernozem, M.A. Surmeneva, B. Krause, T. Baumbach, V.P. Ignatov, O. Prymak, K. Loza, M. Epple, F. Ennen-Roth, A. Wittmar, M. Ulbricht, E. A. Chudinova, T. Rijavec, A. Lapanje, R.A. Surmenev, Functionalization of titania nanotubes with electrophoretically deposited silver and calcium phosphate nanoparticles: structure, composition and antibacterial assay, Mater. Sci. Eng. C 97 (2019) 420–430, https://doi.org/10.1016/j.msec.2018.12.045.

[105] Y. Qing, L. Cheng, R. Li, G. Liu, Y. Zhang, X. Tang, J. Wang, H. Liu, Y. Qin, Potential antibacterial mechanism of silver nanoparticles and the optimization of orthopedic implants by advanced modification technologies, Int. J. Nanomed. 13 (2018) 3311–3327, https://doi.org/10.2147/IJN.S165125.

[106] C.N. Lok, C.M. Ho, R. Chen, Q.Y. He, W.Y. Yu, H. Sun, P.K.H. Tam, J.F. Chiu, C. M. Che, Proteomic analysis of the mode of antibacterial action of silver nanoparticles, J. Proteome Res. 5 (2006) 916–924, https://doi.org/10.1021/pr0504079.

[107] C. Liao, Y. Li, S.C. Tjong, Bactericidal and cytotoxic properties of silver nanoparticles, Int. J. Mol. Sci. 20 (2019) 449, https://doi.org/10.3390/ijms20020449.

[108] Y. Kaneko, M. Thoendel, O. Olakanmi, B.E. Britigan, P.K. Singh, The transition metal gallium disrupts Pseudomonas aeruginosa iron metabolism and has antimicrobial and antibiofilm activity, J. Clin. Invest. 117 (2007) 877–888, https://doi.org/10.1172/JCI30783.

[109] A.K. Crooke, J.R. Fuller, M.W. Obrist, S.E. Tomkovich, N.P. Vitko, A. R. Richardson, CcpA-independent glucose regulation of lactate dehydrogenase 1 in Staphylococcus aureus, PloS One 8 (2013), e54293, https://doi.org/10.1371/journal.pone.0054293.

[110] F. Mat-Jan, K.Y. Alam, D.P. Clark, Mutants of Escherichia coli deficient in the fermentative lactate dehydrogenase, J. Bacteriol. 171 (1989) 342–348, https://doi.org/10.1128/jb.171.1.342-348.1989.

[111] L.R. Bernstein, Mechanisms of therapeutic activity for gallium, Pharmacol. Rev. 50 (1998) 665–682.

[112] A. Hoppe, N.S. Güldal, A.R. Boccaccini, A review of the biological response to ionic dissolution products from bioactive glasses and glass-ceramics, Biomaterials 32 (2011) 2757–2774, https://doi.org/10.1016/j.biomaterials.2011.01.004.